



Calhoun: The NPS Institutional Archive
DSpace Repository

Theses and Dissertations

1. Thesis and Dissertation Collection, all items

1994-06

Multispectral NOAA Marine Atmospheric Boundary Layer (MABL) estimates during VOCAR

Walsh, David J.

Monterey, California. Naval Postgraduate School

<http://hdl.handle.net/10945/28385>

Downloaded from NPS Archive: Calhoun



<http://www.nps.edu/library>

Calhoun is the Naval Postgraduate School's public access digital repository for research materials and institutional publications created by the NPS community. Calhoun is named for Professor of Mathematics Guy K. Calhoun, NPS's first appointed -- and published -- scholarly author.

Dudley Knox Library / Naval Postgraduate School
411 Dyer Road / 1 University Circle
Monterey, California USA 93943

DUDLEY KNOX LIBRARY
RALPH POSTGRADUATE SCHOOL
MONTEREY CA 93943-5101

Approved for public release; distribution is unlimited.

Multispectral NOAA Marine Atmospheric Boundary Layer (MABL) Estimates During VOCAR

by

David J. Walsh
Lieutenant, United States Navy
B.A., University of California, Berkeley, 1979

Submitted in partial fulfillment
of the requirements for the degree of

MASTER OF SCIENCE IN METEOROLOGY AND
PHYSICAL OCEANOGRAPHY

from the

NAVAL POSTGRADUATE SCHOOL
June 1994

REPORT DOCUMENTATION PAGE

Form Approved OMB No. 0704

Public reporting burden for this collection of information is estimated to average 1 hour per response, including the time for reviewing instruction, searching existing data sources, gathering and maintaining the data needed, and completing and reviewing the collection of information. Send comments regarding this burden estimate or any other aspect of this collection of information, including suggestions for reducing this burden, to Washington Headquarters Services, Directorate for Information Operations and Reports, 1215 Jefferson Davis Highway, Suite 1204, Arlington, VA 22202-4302, and to the Office of Management and Budget, Paperwork Reduction Project (0704-0188) Washington DC 20503.

1. AGENCY USE ONLY (Leave blank)	2. REPORT DATE June 1994	3. REPORT TYPE AND DATES COVERED Master's Thesis
----------------------------------	-----------------------------	---

4. TITLE AND SUBTITLE MULTISPECTRAL NOAA MARINE ATMOSPHERIC BOUNDARY LAYER (MABL) ESTIMATES DURING VOCAR	5. FUNDING NUMBERS
---	--------------------

6. AUTHOR(S) David J. Walsh	
--------------------------------	--

7. PERFORMING ORGANIZATION NAME(S) AND ADDRESS(ES) Naval Postgraduate School Monterey CA 93943-5000	8. PERFORMING ORGANIZATION REPORT NUMBER
---	--

9. SPONSORING/MONITORING AGENCY NAME(S) AND ADDRESS(ES)	10. SPONSORING/MONITORIN AGENCY REPORT NUMBER
---	--

11. SUPPLEMENTARY NOTES The views expressed in this thesis are those of the author and do not reflect the official policy or position of the Department of Defense or the U.S. Government.

12a. DISTRIBUTION/AVAILABILITY STATEMENT Approved for public release; distribution is unlimited.	12b. DISTRIBUTION CODE *A
---	------------------------------

13. ABSTRACT (maximum 200 words)
Satellite derived images of surface relative humidity and boundary layer height are generated from AVHRR data collected in a coastal region during the Variability of Coastal Atmospheric Refractivity (VOCAR) IOP (24 August - 03 September 1993) for comparison with in-situ data. The technique, proposed by Kren (1987) and verified by Smolinski (1988) uses channels 1, 4, and 5 via the relationship between radiative extinction and relative humidity. The input variables measured are 1) sea surface temperature, and 2) total atmospheric water vapor, from the split-window technique in addition to 3) aerosol optical depth, inferred from Channel 1 radiance. The assumption of total atmospheric water vapor confined to the MABL is relaxed. Satellite-derived boundary layer heights are brought into agreement with radiosonde measurements by varying the amount of water vapor confined to the MABL. Agreement between satellite and radiosonde measured heights and slopes is good. Spatial and temporal variability of refractive conditions over the region is large. The method appears capable of tracking the bottom of a trapping layer, associated with the inversion at the top of the MABL, inferred from radiosonde measurements. Comparison with the IR Duct Technique, an empirical method which applies to cloudy areas, shows promise for integration with this technique for clear areas.

14. SUBJECT TERMS Remote Sensing, Coastal Meteorology, AVHRR, Marine Atmospheric Boundary Layer, Refractivity.	15. NUMBER OF PAGES 115
---	----------------------------

	16. PRICE CODE
--	----------------

17. SECURITY CLASSIFICATION OF REPORT Unclassified	18. SECURITY CLASSIFICATION OF THIS PAGE Unclassified	19. SECURITY CLASSIFICATION OF ABSTRACT Unclassified	20. LIMITATION OF ABSTRACT UL
---	--	---	----------------------------------

ABSTRACT

Satellite derived images of surface relative humidity and boundary layer height are generated from AVHRR data collected in a coastal region during the Variability of Coastal Atmospheric Refractivity (VOCAR) IOP (24 August - 03 September 1993) for comparison with in-situ data. The technique, proposed by Kren (1987) and verified by Smolinski (1988) uses channels 1, 4, and 5 via the relationship between radiative extinction and relative humidity. The input variables measured are 1) sea surface temperature, and 2) total atmospheric water vapor, from the split-window technique in addition to 3) aerosol optical depth, inferred from Channel 1 radiance. The assumption of total atmospheric water vapor confined to the MABL is relaxed. Satellite-derived boundary layer heights are brought into agreement with radiosonde measurements by varying the amount of water vapor confined to the MABL. Agreement between satellite and radiosonde measured heights and slopes is good. Spatial and temporal variability of refractive conditions over the region is shown to be large. The method appears capable of tracking the bottom of a trapping layer, associated with the inversion at the top of the MABL, inferred from radiosonde measurements. Comparison with the IR Duct Technique, an empirical method which applies to cloudy areas, shows promise for integration with this technique for clear areas.

71515
U2228212
C,1

TABLE OF CONTENTS

I.	INTRODUCTION	1
II.	BACKGROUND	4
	A. ATMOSPHERIC REFRACTION	4
	B. ELEVATED DUCTS	5
	C. EVAPORATION DUCT	6
	D. REMOTE SENSING OF VARIABLES AFFECTING DUCTING .	7
III.	VARIABILITY OF COASTAL ATMOSPHERIC REFRACTIVITY	11
	A. VOCAR ORGANIZATION / OBJECTIVES	11
	B. VOCAR DATA	12
	1. Upper Air	12
	2. Meteorological Station Data	12
	3. Satellite (AVHRR) Data	13
	4. Buoy Data	14
IV.	BACKGROUND / METHODOLOGY	15
	A. MABL CHARACTERISTICS	16
	B. TECHNIQUE ASSUMPTIONS	16
	1. Well-Mixed MABL	17
	2. Optical Depth is Confined to the MABL . . .	18

3.	Total Water Vapor is Confined to the MABL	20
4.	Deriving the Iterative Formulae	21
5.	Relative Humidity Parameterization	24
C.	DETERMINATION OF SURFACE RELATIVE HUMIDITY AND BOUNDARY LAYER HEIGHT	26
1.	Initial Values of the Input Variables	26
2.	Application of the Iterative Scheme	26
D.	REMOTE MEASUREMENT OF INPUT VARIABLES	28
1.	Sea Surface Temperature	28
2.	Total Atmospheric Water Vapor	29
3.	Aerosol Optical Depth	34
E.	CRITERIA FOR SELECTION OF CASE STUDIES	37
1.	Daytime Pass	38
2.	Cloud Free Regions	38
3.	Sunglint	38
4.	Match with Initial Assumptions	38
5.	Gradients Observed in Satellite Images	39
6.	Spatial and Temporal Considerations	39
V.	RESULTS OF SATELLITE ANALYSIS	40
A.	APPROACH	40
B.	MABL CHARACTERISTICS FOR VOCAR	40
C.	CASE STUDIES	42
1.	Case One: 27 August, 1993	42
a.	Visible and Infrared Satellite Images	42
b.	Sea Surface Temperature Image	44

c.	Boundary Layer Height Image	44
d.	Transects of Satellite BL Heights	45
(1)	The Coastal Transect	47
(2)	The Offshore Transect:	48
(3)	The VOCAR Transect	48
e.	M-Index Profiles	49
f.	Surface Relative Humidity Image	51
2.	Case Two: 28 August, 1993	52
a.	Visible and Infrared Satellite Images	52
b.	Sea Surface Temperature Image	53
c.	Boundary Layer Height Image	54
d.	Transects of Satellite BL Heights	54
(1)	The Coastal Transect:	55
(2)	The Offshore Transect:	55
(3)	The VOCAR Transect	56
e.	M-Index Profiles	57
f.	Surface Relative Humidity Image	58
D.	METHOD VERIFICATION	58
1.	Sea Surface Temperature	59
2.	Boundary Layer Height	59
3.	Surface Relative Humidity, RH(0)	60
4.	Comparison With IR Duct Technique	61
VI.	CONCLUSIONS	63
	APPENDIX	66

LIST OF REFERENCES 103

INITIAL DISTRIBUTION LIST 105

ACKNOWLEDGEMENTS

A number of individuals contributed greatly to the completion of this thesis. Professors Carlyle Wash and Kenneth Davidson provided continuous guidance and encouragement. Professor Phil Durkee sparked my interest in remote sensing to begin with. More importantly, support from the Meteorology staff was instrumental. Dick Lind provided the vertical moisture integration program. Kurt Nielsen recovered the original boundary layer height program and moved it to the UNIX environment. Chuck Skupniewicz spearheaded development of the program in it's present form and tutored me in the world of TERASCAN. Mary Jordan assimilated the mother of all sounding and surface observation data sets and generated all the requisite GEMPAK plots. Without their help this project would not have come to fruition! Thanks to my wife Katherine, for being there, and having been there through a fairly demanding Naval schedule.

This thesis is dedicated to my good friend Jeff, who has been, and I'm sure always will be, an inspiration.

I. INTRODUCTION

The current U.S. Navy emphasis on littoral warfare challenges the environmental support from Commander, Meteorology and Oceanography Command. The littoral zone is a region of the ocean where complex air-sea interactions occur. Consequently, atmospheric parameters responsible for refraction show high spatial and temporal variability, influencing the height of the evaporative and elevated ducts. Ducting significantly impacts the performance of shipboard sensors, weapons, and communications systems. Therefore, the ability to quantify and predict the rapid evolution of ducting phenomena, in the littoral, is critical to successful future naval engagements.

Existing systems (sodar and radiosondes) provide information only at the point of measurement. The breadth of battle group operations dictates the need for satellite sensors to provide a larger scale atmospheric analysis in near real-time. Satellite derived refractive estimates would standardize battle group electromagnetic (EM) integration providing our forces an advantage, increasingly important in this era of 'smart-weapons.' The IR Duct technique (Rosenthal and Helvey 1992), based on visual imagery patterns and infrared-derived cloud top temperatures, is an important step in this direction. This

allows one to estimate the height of the bottom of a trapping layer, from which we can infer refractive conditions, for stratus regions.

Key to remote sensing of refractive conditions is the ability to accurately retrieve the parameters responsible for anomalous refraction (negative vertical humidity gradient and / or positive vertical temperature gradient). The difficulty lies in the fact that we are interested in these variables at the bottom of the marine atmospheric boundary layer (MABL) where satellite data is generally less reliable. Any demonstrated relationship between other retrievable parameters and refractive conditions must also be included in the technique.

Sea surface and surface air temperatures can be estimated in clear regions using Advanced Very High Resolution Radiometer (AVHRR) thermal infrared (IR) data. Satellite derived images representing atmospheric water vapor are achieved via differences in brightness temperatures between the split window channels (AVHRR CH4 and CH5), a technique first described by Dalu (1986). Multispectral techniques (Kren 1987, Smolinski 1988) provide estimates of boundary layer height and surface relative humidity and map these spatially over a region. The relationships of these fields to refractive conditions motivates this investigation.

Data from the Variability of Coastal Atmospheric Refractivity (VOCAR) Intensive Observation Period (IOP), August - September 1993 from the southern California bight will be used in this thesis. The purpose of this thesis will be:

- to construct satellite derived images of boundary layer height and surface relative humidity using the Kren/Smolinski algorithm, and atmospheric water vapor images with the (AVHRR) CH4 - CH5 technique.
- to evaluate the usefulness of the above images by attempting to locate patterns in the satellite analysis related to those observed in both in-situ radiosonde and surface observation data.
- to use these satellite boundary layer analysis techniques to estimate atmospheric refractive effects.

II. BACKGROUND

A. ATMOSPHERIC REFRACTION

An electromagnetic (EM) signal propagating through the atmosphere will undergo absorption and re-emission or scattering of EM energy. This is a result of variations in the vertical distribution of atmospheric moisture and temperature. These variations create gradients in refractivity, changing propagation velocity, which leads to a bending of the signal path. This bending, called refraction, can significantly alter the range (horizon) over the curved earth a signal might travel. When the ray is bent upward, a condition known as subrefraction, the horizon distance will be reduced. An increased horizon may result from superrefraction, the situation where the ray is bent significantly downward, and tends to follow the curvature of the earth. In the case of a trapping layer the ray is refracted (relative to the earth) upward in the bottom of this layer and downward at the top of the layer. The signal is effectively trapped and may propagate over great distances. Figure 1 illustrates each of these cases.

B. ELEVATED DUCTS

To clearly indicate the presence of trapping layers within the atmosphere, a modified index is used. This modified index, called the M-index, is defined as

$$M=N+(\cdot 157m^{-1})(z) \quad (1)$$

(where N is the value of refractivity at any height z, in meters.) Martinez (1991) provides a detailed explanation of refractivity (N). The importance of the modified (M-index) is that dM/dz must be negative for a trapping layer to form. A trapping layer is likely to form where humidity decreases rapidly with height and / or temperature increases rapidly with height. A duct is the region associated with a trapping layer in which the EM energy is trapped. The duct may be of two types: 1) elevated duct, or 2) surface based duct, as shown in Figures 2 (a), (b) and (c). The top of each type of duct will always be at the same height as the top of the trapping layer. However, the bottom of each duct will generally extend below the bottom of the trapping layer. The elevated duct will have it's lower boundary above the surface while that of the surface based duct will be at the surface.

The top of the typical marine atmospheric boundary layer (MABL) is characterized by a large decrease in specific humidity and a large increase in potential temperature -

ideal for formation of a trapping layer. This trapping layer, if it remains above the surface, will result in an elevated duct. Shipboard EM signals originating within this duct may experience greatly increased ranges (horizon) as a result of trapping. As the signal energy is generally contained within the duct, targets outside of this layer, in the case of radar systems, may go undetected. This represents a substantial problem for shipboard radar operators, particularly those attempting to detect and track low-flying anti-ship cruise missiles.

Temporal and spatial variations in trapping layers and elevated ducts are observed on time scales of a few hours, particularly in the coastal environment. Martinez (1991) observed that, along the central California coast, frontal passage can have a significant effect on the presence and location of any trapping layers. He found that for a given location refractive conditions are highly variable in space and time, and current refractive models do not accurately indicate the complexity of refractive conditions often observed.

C. EVAPORATION DUCT

A thin surface-based duct often forms over the sea as a result of a humidity decrease immediately above the surface; with typical heights of 2 - 30m. For comparison, such a duct would occupy roughly 5-20% of the depth of the surface

based duct shown in Figure 2c. This evaporation duct is due to a negative vertical humidity gradient at the surface and is possibly enhanced by a positive temperature gradient. The height of the evaporation duct is generally less than can be resolved by radiosonde; average heights place the evaporative duct below the level of most U.S. Naval combatant radar, sensor, and communications antennae. However, this is not always the case; units underway must be aware of any changes in local refractive conditions.

Previous studies confirm the variable nature of the evaporative duct. Geernaert (1989) indicated that current approaches to assessing refraction, assuming horizontal homogeneity, are unrealistic. He points out that successful modeling of the ray path requires a smaller scale than presently contained in numerical weather prediction systems. The scale depends upon sea surface temperature (SST) variability and local weather features. For example, in the presence of sea fog, under stable and light wind conditions an evaporation duct will be capped by a strong, positive temperature gradient, producing an even deeper surface based duct. He concluded that regions with warm SST may exhibit deep surface evaporation ducts as a result.

D. REMOTE SENSING OF VARIABLES AFFECTING DUCTING

Numerous investigators have employed methods for remotely sensing the parameters responsible for, and / or

possibly related to, refraction. Some of these methods are direct, others based on indirect measurements. Regardless, remote sensing of conditions affecting duct occurrence should be possible in clear regions of the littoral zone using NOAA's AVHRR.

Kren (1987) presented an indirect method which requires a measurement of aerosol optical depth, total water vapor, and SST, using the relationship between relative humidity and radiative extinction to estimate MABL depth and surface relative humidity. The advantage of this technique is that all measurements are made with the same satellite sensor, along the same optical path, eliminating resolution conflicts and the need for data integration.

Two necessary assumptions for the method to be accurate are: 1) all aerosols contributing to radiative extinction must be located in the MABL, 2) all water vapor which contributes to integrated water vapor must be contained in the MABL. Whereas these conditions may represent a well-mixed MABL; they can often be violated. The procedure should give accurate results in regions of : 1) cloud free atmospheres, 2) subtropical anticyclones, 3) away from continental aerosols, and 4) whenever minimal water vapor exists above the MABL. If the atmosphere matches these assumptions, estimates of MABL depth and surface relative humidity are possible. As the atmosphere deviates from these conditions so does the accuracy of the estimates.

Smolinski (1988) verified the feasibility of the method and confirmed the results of Kren (1987). He also incorporated a technique for spatially mapping boundary layer depth and surface relative humidity within the satellite swath. Although Smolinski found no strong correlation between surface relative humidity and boundary layer depth, he did note that lower surface relative humidity is found in regions of greater boundary layer depth. The technique for estimating humidity shows a significant bias for overestimation, in nine of ten verification cases, as a result of a portion of the total water vapor being above the boundary layer.

Rosenthal and Helvey (1992) employed the IR Duct Technique with some success in the Persian Gulf. The technique provides a potentially automated means of mapping the propagation environment for use in operational Navy applications. Visual imagery patterns are used to infer the occurrence of ducts, and IR imagery is used to infer the spatial distribution of duct heights. IR brightness values are used to calculate cloud-top temperatures. The method applies over the open ocean in subtropical inversion-dominated regions typically covered by stratus and stratocumulus clouds. Seasonal mean profiles, based on statistics from over 4000 radiosondes, form the basis for converting cloud top temperature to a calculated height of duct base. Sea surface temperatures have a major impact on

these seasonal profiles and resultant duct heights, so were included as geographic and seasonal factors in the algorithm.

Geernaert (1989) reports that the full boundary layer rapidly adjusts to changes in sea surface temperature (SST). He proposes the use of a large aperture microwave radiometer for evaluating evaporation ducts. The radiometer could be used to provide information on both the magnitude and variability of SST. This is possible because, if we assume the air near the ocean surface to be saturated, then SST determines the specific humidity of that air. One must couple SST patterns with wind speed and direction to determine if the flow is toward or away from colder waters. The impact of flow toward colder water is much more dramatic in terms of refractive effects. Wind vectors can be estimated by using SSM/I fields overlayed with surface pressure analyses from Fleet Numerical Meteorology and Oceanography Command (FNMOC).

To provide on-line duct information processing, a scatterometer would be required or a synthetic aperture radar (SAR) to resolve fine-scale variability. He concludes that, in the case where surface conditions are not horizontally homogeneous, calculating boundary layer depth is particularly important for estimating the spatial variability of relative humidity.

III. VARIABILITY OF COASTAL ATMOSPHERIC REFRACTIVITY

A. VOCAR ORGANIZATION / OBJECTIVES

VOCAR is a multi-group effort to investigate the mesoscale variability of atmospheric refractivity with emphasis on the coastal zone. The objective of VOCAR is to provide an assessment capability for horizontally varying refractivity conditions in a coastal environment. The Intensive Observation Period was conducted 24 August - 03 September 1993 in the southern California bight. Naval Postgraduate School (NPS) participation focused upon observations from R/V Pt. Sur. The Pt. Sur was both a surface and upper-air observation platform; in addition, NPS conducted satellite image analysis in conjunction with in-situ measurements. The NPS goal is to evaluate the value of digital satellite data in the assessment of refractive conditions over the region.

The unique nature of VOCAR stems from the wide variety of environmental sensors employed, the density of the station network, and the frequency of observations. These combined to provide a high spatial and temporal resolution of the atmospheric variables responsible for refraction. This was the result of a great deal of coordination and cooperation amongst a large number of participants. The

next section discusses only that portion of the data collected during the IOP which was utilized for this thesis.

B. VOCAR DATA

1. Upper Air

A very significant aspect of VOCAR; radiosonde launches every four hours were conducted at eight locations shown in Figure 3, from (12Z) 23 August to (00Z) 04 September 1993. Balloon ascent rates were reduced in an effort to concentrate data collection within the marine atmospheric boundary layer. These soundings were sampled every five seconds, approximately every 10 - 15 meters, up to 500 observations. From this data N (refractivity), M (modified index of refraction), and dM/dz (rate of change of M with height) were computed.

2. Meteorological Station Data

In addition to the above eight radiosonde locations, standard meteorological observations were available from dozens of stations along the coast and / or offshore in the VOCAR region. These included: 1) air temperature, 2) wind speed and direction, and, in some cases, 3) dewpoint temperature or 4) relative humidity and, 5) sea level pressure. R/V Pt. Sur also provided continuous surface and aerosol measurements.

Hourly data from these locations was plotted on a standard Mercator projection of the region for comparison

with satellite images. The list of surface stations utilized for this study is shown in Table 1.

3. Satellite (AVHRR) Data

A total of fifty satellite passes (NOAA 11 & 12) were collected at NPS during the VOCAR IOP. AVHRR sensor datasets were created from high resolution picture transmission (HRPT) telemetry data. All five AVHRR channels were archived throughout the period:

- Channel 1, 0.58 - 0.68 μm , red-visible,
- Channel 2, 0.72 - 1.10 μm , red-visible/near infrared,
- Channel 3, 3.55 - 3.93 μm , near infrared,
- Channel 4, 10.3 - 11.3 μm , thermal infrared,
- Channel 5, 11.5 - 12.5 μm , thermal infrared.

Upon downloading the data, bad or missing lines were duplicated from neighboring good lines, up to a maximum of two adjacent missing lines. AVHRR sensor counts were converted to values with engineering units, a process referred to as radiometrically calibrating the data. For channels 1 and 2 the units are percent albedo; for channels 3 to 5 the units are brightness temperature. The images were then registered to a base map and projection using a master file of the VOCAR region for standardization. In every subsequent comparison with in-situ data an attempt was

made to minimize the time difference between satellite pass and observation.

4. Buoy Data

NOAA operates five meteorological buoys in the VOCAR region, at the locations indicated by a five-digit symbol (eg. 46053) in Figure 3. The data utilized from these buoys consisted of: 1) sea level pressure, 2) air temperature, 3) wind speed and direction, and 4) sea surface temperature. The data from these buoys, as well as any ship reports from the area during the VOCAR IOP, were archived in the NPS Interactive Digital Environmental Analysis (IDEA) Lab. This information was combined with the meteorological stations (above) to comprise the complete surface data set for this thesis.

It is important to note that the NOAA buoys do not have any humidity sensors. This prevents the calculation of spatial evaporation duct heights using NOAA buoy observations. This was only accomplished in the vicinity of Pt. Sur using ship surface observations.

IV. BACKGROUND / METHODOLOGY

Kren (1987) proposed, and Smolinski (1988) verified that the height of the MABL and the surface relative humidity may be indirectly estimated using visual and IR satellite data. The advantages of the technique are twofold: First, all data comes from the same sensor (AVHRR) along the same optical path, eliminating resolution conflicts and the need for data integration. Secondly, the methods for determining the input variables (optical depth, total atmospheric water vapor, sea surface temperature, and sea level pressure) are all understood and well documented. The disadvantage of the technique is that each of these remote sensing procedures requires a cloud-free atmosphere, not always present in the coastal region. Assuming the MABL is well mixed, with aerosols and water vapor contained therein, the four variables above can be utilized to estimate boundary layer height and surface relative humidity using an iterative process.

In this chapter, the characteristics of a well-mixed MABL will be discussed and compared to the conditions observed during VOCAR. The accuracy of assumptions concerning the distribution of both aerosols and water vapor will be examined. The parameterization of relative humidity and the iterative procedure for determining surface relative

humidity and boundary layer height (including the initial values of the input variables) will be explained. The methods for remotely sensing sea surface temperature, total water vapor, and optical depth will be reviewed.

A. MABL CHARACTERISTICS

The typical unstable marine atmospheric boundary layer can be separated into three regions as shown in Figure 4. The surface layer is normally characterized by a superadiabatic lapse rate, moisture decrease with height, and strong wind shear. The mixed layer is so named because intense vertical mixing tends to leave conserved variables such as potential temperature and humidity nearly constant with height. Rogers (1979) describes the ongoing process whereby samples of air are brought adiabatically to the same pressure level and mixed, maintaining these constant moisture profiles. The inversion layer is the region of statically stable air at the top of the mixed layer where large gradients of temperature and moisture are often observed, the result of subsidence above into the boundary layer.

B. TECHNIQUE ASSUMPTIONS

The Kren / Smolinski technique is based on three assumptions about the MABL:

- The MABL values of potential temperature and specific humidity are well mixed.
- Aerosol optical depth at red-visible and near infrared wavelengths results from particles confined to the MABL.
- Total atmospheric water vapor is confined to the MABL.

The validity of each of these assumptions will be discussed and compared with conditions observed during the VOCAR IOP.

1. Well-Mixed MABL

Turbulent mixing within the layer can be generated convectively by buoyancy or mechanically by wind shear. Buoyant production occurs whenever the underlying surface is warmer than the air above. Over the sea surface, this is particularly true at night, when the high heat capacity of the ocean allows it to remain warmer than the near surface air which cools quickly after sunset. Convective eddies caused by surface heating together with wind shear-induced eddies are effective in transferring heat away from the warm sea surface. Shear production is often associated with the surface layer because of its limited vertical extent. The combination of buoyancy and shear production generally results in a well-mixed boundary layer. The most remarkable feature of the well-mixed boundary layer is the jump in potential temperature (increase) and humidity (decrease) at the top, Businger (1985).

Figures 5 (a) and (b) are soundings from the PT. Sur taken at 2352Z, 28 August 1993, in the center of the VOCAR

region. The profiles indicate nearly constant values of potential temperature and mixing ratio within the boundary layer, from the surface to approximately 400m. At the top of the inversion capped boundary layer the jump in both parameters is also observed. This is an example of the extent to which in-situ conditions support the assumption of a well-mixed MABL. Smolinski (1988) indicated that the further conditions deviate from the assumption of a well-mixed MABL, the greater the error in the estimates of surface relative humidity and boundary layer height. During the VOCAR IOP, the MABL was usually well-mixed; a time series of potential temperature and mixing ratio from the Pt. Sur, will be presented later.

2. Optical Depth is Confined to the MABL

As a parameter, optical depth encompasses a wide variety of physical processes. Vertical optical depth is defined as the vertical integral of the extinction coefficient through the depth of the atmospheric column:

$$\tau = \int_0^{z_{\text{top}}} \beta_{\text{ext}} dz \quad (2)$$

Since extinction coefficient has units of km^{-1} and is integrated over dz , optical depth is a dimensionless quantity that describes the amount of attenuation within the

atmosphere. The extinction coefficient was reported by Shettle and Fenn (1979) to be defined for atmospheric aerosol distributions as:

$$\beta_{ext} = \int_0^{\infty} \pi r^2 Q_{ext}(m, r) n(r) dr \quad (3)$$

where:

- πr^2 = cross sectional area for a given radius,
- $Q_{ext}(m, r)$ = extinction efficiency (a function of the complex refractive index and particle radius), and
- $n(r)$ = distribution of particles by radius.

Kren (1987) gave a detailed analysis of the effects of variations of these three factors and corresponding changes in extinction. Fitzgerald et al. (1982) reported that the dominant term affecting extinction is particle size. Durkee (1984) confirmed the relationship between extinction and relative humidity consistent with Fitzgerald's work. The result was the expression, illustrated in Figure 6:

$$\beta_{ext} = \frac{1}{A(B - RH)} \quad (4)$$

where $A = .2998 \text{ km}/\%$, $B = 99.8999\%$, and RH = relative humidity. The relationship is based on aircraft measurements of extinction within the MABL off the southern California coast, in the VOCAR region. Figure 7 shows the profiles of extinction, relative humidity and potential

temperature for 5 October 1982 off the coast of California (Durkee, 1984). As can be seen from the extinction profile, the majority of optical depth is confined to the boundary layer.

Koepke and Quenzel (1981) report that ocean surface reflections contribute little to upwelled radiance at wavelengths used to measure optical depth on the AVHRR (CH1 - $0.63\mu\text{m}$.). By limiting the application of the technique to well-mixed regions when sunglint is negligible, and by using channel 1 of the AVHRR, the assumption of optical depth confined to the MABL is well supported.

3. Total Water Vapor is Confined to the MABL

The total water vapor content in a column of atmosphere is defined as the vertical integral of the vapor density within the column. Under the assumption that the total water vapor is confined to the MABL, the vapor density must also be confined to the MABL and the integration distance becomes the depth of the boundary layer,

$$W = \int_0^{\Delta z} \rho_w(z) dz. \quad (5)$$

Nieman (1977) discusses maritime air masses associated with a strongly subsiding troposphere. Over oceanic regions, the lower troposphere is moistened by fluxes across the air-sea interface, resulting in a moist MABL beneath a dry, free

troposphere. The water vapor content above the subsidence inversion is minimized and the assumption of total water vapor being confined to the MABL is reasonable under these conditions. Nevertheless, a significant problem exists in the present technique because a portion of the total water vapor may reside above the boundary layer. This is true of the VOCAR period in particular. This deviation from initial assumptions results in overestimates of surface relative humidity. The next chapter will include a discussion of an attempt to correct for this inaccurate assumption.

4. Deriving the Iterative Formulae

For the purpose of deriving the iterative formulae it is assumed that both aerosol optical depth and total water vapor are confined to the MABL; then the integration distance is the depth of the boundary layer which is the same for both variables. Starting with the definition for optical depth,

$$\tau = \int_0^{\Delta z} \beta_{ext} dz, \quad (6)$$

and using the relationship between extinction and relative humidity (Durkee, 1984),

$$\beta_{ext} = \frac{1}{A(B - RH)} \quad (7)$$

where $A = .2998 \text{ km/\%}$ and $B = 99.8999\%$, one can substitute equation 7 into equation 6 and solve for optical depth,

$$\tau = \frac{1}{A} \int_0^{\Delta z} \frac{1}{(B - RH(z))} dz \quad (8)$$

where A and B are defined above, $RH(\Delta z)$ is relative humidity at the top of the MABL and $RH(0)$ is surface relative humidity. Using a linear parameterization for relative humidity, explained further in the next section,

$$RH(z) = RH(0) + Cz \quad (9)$$

and integrating equation 8 over the depth of the boundary layer yields

$$\tau = -\frac{1}{AC} \ln \left[\frac{B - RH(0) - C\Delta z}{B - RH(0)} \right]. \quad (10)$$

If we solve equation 10 for Δz , boundary layer depth becomes:

$$\Delta z = \frac{B - (B - RH(0)) e^{-\tau AC} - RH(0)}{C}. \quad (11)$$

Next, starting with the definition for total water vapor,

$$W = \int_0^{\Delta z} \rho_w(z) dz \quad (12)$$

and relative humidity,

$$RH = \frac{\rho_w}{\rho_{ws}} \times 100\% \quad (13)$$

we rearrange equation 13 and substitute into equation 12 to obtain:

$$W = \int_0^{\Delta z} \frac{RH(z) \rho_{ws}(T)}{100} dz. \quad (14)$$

We must next assume a constant mean layer vapor density, following the well-mixed MABL assumption, so

$$W = \frac{[RH(\frac{\Delta z}{2}) \rho_{ws}(T(\frac{\Delta z}{2}))]}{100} \Delta z. \quad (15)$$

Utilizing, again, the relative humidity parameterization, equation 15 becomes:

$$W = \frac{[(RH(0) + C(\frac{\Delta z}{2})) \rho_{ws}(T(\frac{\Delta z}{2}))]}{100} \Delta z. \quad (16)$$

Solving equation 16 for Δz gives:

$$\Delta z = \frac{-RH(0) \pm \sqrt{[RH(0)^2 + 200CW\rho_{ws}(T_{lyr})]}}{C} \quad (17)$$

In equation 17 the positive root of the radical is always selected to provide the meteorologically sensible solution. If we now combine equations 17 and 11 through the common factor Δz , this leads to a quadratic equation in surface relative humidity, $RH(0)$,

$$(1 - (e^{-\tau AC})^2) \times RH(0)^2 + (2Be^{-\tau AC}(e^{-\tau AC} - 1)) \times RH(0) - B^2(1 - e^{-\tau AC})^2 + \frac{2 \times 10^{-3}}{\rho_{ws}(T_{lyr})} = 0, \quad (18)$$

as a function of optical depth, saturation vapor density, and the relative humidity parameter C. The other equation upon which the technique iterates is equation 11 (above), the solution for boundary layer depth.

5. Relative Humidity Parameterization

The variable C in equation 18 describes the percentage increase in relative humidity from the near-surface value, to the top of the layer, normalized to 1000m. This can be thought of as a relative humidity lapse rate. In deeper layers, because of the substantial temperature change through the depth of the layer, the nonlinearity of the saturation vapor density function influences the relative humidity profile. For thin layers (<1 km) the saturation vapor density function is nearly linear and the relative humidity profile can be approximated

by a straight line. The parameterization is a linear function with height:

$$RH(z) = RH(0) + Cz \quad (19)$$

where $RH(z)$ is the relative humidity at any height z , $RH(0)$ is surface relative humidity and C describes the percentage increase in relative humidity with height. Surface relative humidity is defined as the extrapolation of the linear relative humidity profile down to zero meters.

Theoretically, the surface relative humidity over the ocean is always 100%, however for the purpose of parameterizing the relative humidity lapse rate, the above definition of the extrapolated value is used. Kren (1987) examined variations in boundary layer depth and found a functional relationship:

$$C = 14.07 + 3.333(\Delta z) \quad (20)$$

where Δz is the layer thickness in km and C is in dimensions of %/km. Smolinski (1988) discovered that variations in SST and surface relative humidity also effect the value of C . He compared constant and changing values of the relative humidity lapse rate and found little difference in the sensitivity of the parameters when the variable lapse rate was taken into account. In addition, the variable lapse rate method is considerably slower - computationally. The

increase in computational time offsets the near negligible improvement in accuracy. In an effort to provide near real-time estimates of surface relative humidity and boundary layer height the simpler lapse rate (20) is utilized here.

C. DETERMINATION OF SURFACE RELATIVE HUMIDITY AND BOUNDARY LAYER HEIGHT

1. Initial Values of the Input Variables

The input variables for the iterative scheme take on the following initial values:

- $C=14.07+3.333(\Delta z)$
- $W=1.96(T_4-T_5)\cos\theta$, from McMillin and Crosby (1984) use of split window data, more detail follows.
- $SST=0.877(T_4)+0.0831(T_4-T_5)T_{sfc}+0.349(T_4-T_5)(\sec\theta-1)$
 $:T_{sfc}=0.963(T_4)+2.679(T_4-T_5)+0.242(T_4-T_5)(\sec\theta-1)-263.0$
 from current NOAA daytime, split window, nonlinear SST equations.
- $\rho_{ws}=\frac{6.11\times 10^{\frac{(7.5\times T)}{(T+237.3)}}\times 10^{-4}}{R_v\times (T+273.16)}$, where $T = SST$, initially, and
 $R = .461 \text{ J/K-g.}$
- $\tau=\frac{4\mu L_A}{\omega_o F_o p(\theta)}$, following Durkee's (1986) analysis, more detail follows.

2. Application of the Iterative Scheme

Figure 8 summarizes the sequence of events to determine surface relative humidity and boundary layer height as well as producing an image of these fields over a region. The above initial values of the input variables are

used to solve equation 18 for $RH(0)$. This $RH(0)$ value is then substituted into equation 11 to solve for Δz . This initial boundary layer height is used to refine the value of C in equation 20. Successive values of saturation vapor density (ρ_{ws}) are mid-layer values as the hypsometric formula and Poisson's equation are applied to the computed layer thickness and temperature respectively. The initial MABL height is subdivided into four equal sublayers and the hypsometric formula is applied to determine the pressure at the top of the first sublayer:

$$P_{i+1} = P_i e^{-\frac{g \Delta Z_s}{RT_v}} \quad (21)$$

where P_i and P_{i+1} are pressures at the bottom and top of the sublayer respectively, g is the acceleration of gravity and R is the universal gas constant. This step is initiated by an estimate of the surface pressure, assumed 1025 mb, the mean layer virtual temperature and knowledge of the sublayer thickness.

Poisson's equation enables the computation of temperature at the top of the sublayer:

$$T_{i+1} = T_i \left(\frac{P_{i+1}}{P_i} \right)^{(.286)} \quad (22)$$

A second use of the hypsometric formula and Poisson's equation on the second sublayer enables the computation of

the mid-layer temperature. This temperature is the basis for the layer vapor saturation density.

The mean sublayer virtual temperature is not actually available due to the lack of moisture information required for it's determination. A reasonable approximation may be found by using the temperature at the bottom of the sublayer. The error is minimized, since virtual temperature typically exceeds the ambient air temperature by a few degrees Centigrade due to atmospheric moisture, and the temperature at the bottom of the sublayer exceeds the mid-layer temperature due to the adiabatic lapse rate.

Since saturation vapor density and the relative humidity lapse rate are variables in the quadratic equation for surface relative humidity, iteration is required. The technique is considered to have converged when the change in MABL depth between successive iterations reduces to less than 10 m.

D. REMOTE MEASUREMENT OF INPUT VARIABLES

1. Sea Surface Temperature

Schwarzchild's equation is the form of the radiative transfer equation concerning a non-scattering, absorbing medium that governs measurement of sea surface temperature. This is a good assumption in the infrared portion of the spectrum in the absence of clouds. The generalized form from Liou (1980) is given by:

$$L_{\lambda}(s_1) = L_{\lambda}(0) e^{-\tau_{\lambda}(s_1, 0)} + \int_0^{s_1} B_{\lambda}[T(s)] e^{-\tau_{\lambda}(s_1, s)} \alpha_{\lambda} ds \quad (23)$$

where:

- $L_{\lambda}(s_1)$ = radiance measured at $s = s_1$,
- $L_{\lambda}(0)$ = radiance emitted at $s = 0$,
- $B_{\lambda}[T(s)]$ = blackbody emission from s ,
- $\tau_{\lambda}(s_1, s)$ = optical depth between points s_1 and s ,
- α_{λ} = absorptance.

Satellite detected radiance will be less than surface emitted radiance as a result of absorption by atmospheric water vapor. This is because the atmosphere is colder than the sea surface and therefore reemits at lower temperature. Corrected sea surface temperatures are achieved by splitting the 10 - 13 μm window to take advantage of differential water vapor absorption across that region. The differential absorption is then used to correct for water vapor attenuation. McClain (1985) reviewed the range of operational MCSST algorithms and reported an rms error of approximately 0.5 °C.

2. Total Atmospheric Water Vapor

The spatial and temporal variability of water vapor make it difficult to measure by remote sensing. The technique is related to a method for the measurement of SST,

mentioned above. Prabhakara et al. (1974), instead of correcting for water vapor absorption, as in the SST measurement, use the varying degrees of absorptance to provide information about the amount of water vapor present in the MABL.

Schwarzchild's equation also serves as the governing relationship for the estimation of atmospheric water vapor. For the 10 - 13 μm spectral range Prabhakara et al. (1974) showed that Schwarzchild's equation can be approximated in terms of brightness temperature as:

$$T_B(\lambda, \theta) = T_s \tau_o(\lambda, \theta) + \bar{T}(\lambda) [1 - \tau_o(\lambda, \theta)] \quad (24)$$

where:

- $T_B(\lambda, \theta)$ = brightness temperature at the top of the atmosphere,
- T_s = surface temperature,
- $\bar{T}(\lambda)$ = mean radiative temperature of the atmosphere,
- $\tau_o(\lambda, \theta)$ = total atmospheric transmittance.

For this application the first channel should be chosen in the most transparent part of the window (to preserve the maximum information about near surface water vapor).

Dalu et al. (1981) proposed a non-linear algorithm for the atmospheric absorption correction to derive sea surface temperature:

$$T_s - T_1 = g(W) (T_1 - T_2) \quad (25)$$

where T_s = sea surface temperature, T_1 = brightness temperature of the most transparent channel, and T_2 = brightness temperature of the second channel, which ideally would have a weighting function with a maximum at the same altitude as the water vapor scale height. $g(W)$ is a function of total water vapor content, and is defined:

$$g(W) = \frac{1 - \tau_1}{C(1 - \tau_2) - (1 - \tau_1)} \quad (26)$$

where $C = (T_s - \bar{T}_2) / (T_s - \bar{T}_1)$ is a constant, τ_1, τ_2 are the total atmospheric transmittances for the two channels.

Equation 25 can thus be further approximated as (Prabhakara et al. 1974):

$$T_s - T_1 \approx (T_s - \bar{T}_1) kWsec\theta \quad (27)$$

where k is equivalent to an absorption coefficient. Equations 25 and 27 can then be combined to yield an expression for total water vapor in terms of the brightness temperature difference of the two channels:

$$T_1 - T_2 \approx \frac{k(T_s - \bar{T}_1)}{g(W)} W \sec \theta \quad (28)$$

Using a radiative transfer model, Prabhakara et al. (1979) verified that the ratio $(T_s - \bar{T}_1)/g(W)$ remains approximately constant in the range of typical atmospheric water vapor contents.

The total water vapor content (W) in a column of atmosphere is the vertical summation of the vapor density (ρ_w) within the column. Returning to our assumption of total atmospheric water vapor confined to the MABL, the vapor density must also reside in the MABL, and the integration distance (Δz) represents the depth of the MABL:

$$W = \int_0^{\Delta z} \rho_w(z) dz \quad (29)$$

The AVHRR channels utilized are CH4 and CH5, with CH4 being the most transparent. McMillin and Crosby (1984) found the atmospheric absorption correction $(T_s - T_4)$ to be a linear function of the brightness temperature difference $(T_4 - T_5)$:

$$T_s - T_4 = a(T_4 - T_5) + b \quad (30)$$

For these channels, equation 27 may be further simplified:

$$W = a(T_4 - T_5) \cos \theta \quad (31)$$

where $a = g(W) / [k(T_s - \bar{T})]$ remains nearly constant for typical atmospheric water vapor levels.

Dalu (1986) found a linear relationship between water vapor content and brightness temperature difference, as shown in Figure 9. From the slope of the line we can determine: $a = 19.6 \text{ kg} / (\text{K} \cdot \text{m}^2)$. This is the result of applying Dalu's technique to a radiative transfer model for a wide range of temperature / humidity profiles, with $\theta = 0$ and $RH(0) = 80\%$. The correlation coefficient $R = 0.99$ and the error is $\pm 1.5 \text{ kg} / \text{m}^2$.

Dalu also simulated AVHRR channel 4 and 5 water vapor retrievals and compared these to ship measured data. The error increases to $\pm 4 \text{ kg} / \text{m}^2$ and the correlation coefficient drops to $R = 0.78$ due to the choice of AVHRR channels, which were not optimized for water vapor retrieval; the channels are too close together.

Dalu (1986) compared ship data and calculated water vapor for situations when surface relative humidity varied from the 80% assumed value. He reported that errors in retrieved water vapor may be minimized if surface relative humidity is known. The correction to be applied can be determined from the regression drawn to the data points in Figure 10. This surface relative humidity correction would

increase the accuracy of the water vapor measurements to approximately $\pm 1.5 \text{ kg/m}^2$.

3. Aerosol Optical Depth

This discussion follows Durkee et al., (1986). Within the cloud-free, marine environment the optical depth due to scattering is small and single scattering processes dominate radiation transfer. Assuming solar radiation is the only intensity source, if we consider the radiation scattered only once by marine aerosols, the radiative transfer equation (Liou, 1980) becomes:

$$L_A = \frac{\omega_o \mu_o F_o}{4 (\mu + \mu_o)} p(\theta) \{1 - \exp[-\tau_A (\frac{1}{\mu} + \frac{1}{\mu_o})]\} \quad (32)$$

where

- L_A = upwelling radiance due to aerosol scattering,
- τ_A = optical depth due to aerosol scattering,
- ω_o = single-scattering albedo,
- $\mu = \cos\theta$, where θ is the satellite zenith angle,
- $\mu_o = \cos\theta_o$, where θ_o is the solar zenith angle,
- $p(\theta)$ = scattering phase function, where θ is the scattering angle,
- F_o = incoming solar radiative flux.

The single-scattering approximation applies for atmospheres with small optical depths. If $\tau_A[(1/\mu)+(1/\mu_o)] \ll 1$, equation 32 reduces to

$$L_A \approx \frac{\omega_{oF_o}}{4\mu} p(\theta) \tau_A \quad (33)$$

From equation 33 it appears that reflected intensity due to single scattering by an optically thin atmosphere is a nearly linear function of τ_A . If the particles are weakly absorbing ($\omega_o \sim 1$, true for marine particles) and F_o is constant, the slope of the relationship depends on $p(\theta)$ and the satellite view geometry through μ .

Optical depth is defined as the vertical integral of the extinction coefficient over the column:

$$\tau_A = \int_0^{\Delta z} \beta_{ext} dz \quad (34)$$

where the extinction coefficient is defined by:

$$\beta_{ext} = \int_0^\infty \pi r^2 Q_{ext}(m, r) n(r) dr. \quad (35)$$

Extinction efficiency, Q_{ext} is calculated from Mie theory and is a function of the complex index of refraction m , wavelength, and particle radius r .

A program written by Wiscombe (1979, 1980) can be used to calculate Q_{ext} , ω_0 , and $p(\theta)$ for the size distributions. The m value depends on relative humidity in the work by Shettle and Fenn (1979). Aircraft or rawinsonde measurements of relative humidity can, therefore, be used to determine m .

Various contributions to the satellite detected, upwelling radiance must be removed to determine the contribution from aerosol particles. After Gordon and Clark (1980), the radiance at satellite altitude (L_S) can be approximated as a sum of independent terms:

$$L_S = (L_W + L_G) \tau + L_R + L_A \quad (36)$$

where L_W is the "water leaving" radiance caused by subsurface, nonspecular reflectance, L_G is specularly reflected radiance at the ocean surface (commonly called sun glint), and τ is the atmospheric transmittance. L_R is the path-added radiance due to Rayleigh scattering in the atmosphere, and L_A is the path-added radiance due to aerosol scattering. L_A is the term of interest, so the magnitude and variation of the remaining terms are needed to estimate L_A from measurements of L_S .

The L_w term is a strongly varying function of wavelength. At blue wavelengths the albedo of the ocean is about 5-10%. At red wavelengths the albedo is less than 0.5% and is zero for wavelengths greater than $0.7\mu\text{m}$ (Ramsey, 1968). Since we are using red to near-infrared wavelengths, L_w will generally be a small contribution to upwelling radiance.

Values of L_G can be estimated from knowledge of sun-earth-satellite geometry and surface roughness. L_G is negligible under all but a small set of geometries McClintock et al. (1971).

The L_R term varies with wavelength but is spatially quite constant. That is, L_R will not cause large variations in L_S except over large regions where geometry changes appreciably. The Rayleigh optical depth τ_R can be estimated from rawinsondes using vertical temperature and pressure profiles. The two-stream model described by Kaufman (1979) and Isaacs (1980) is then used with the values of τ_R to estimate L_R .

E. CRITERIA FOR SELECTION OF CASE STUDIES

A variety of criteria were applied in order to select specific case studies for intensive examination. Some of these are prerequisites for accurately measuring input

variables, others serve as attempts to develop systematic methodologies to apply the technique.

1. Daytime Pass

Aerosol optical depth is estimated using Channel 1 albedo; this necessitates a daytime satellite pass as Channel 1 is in the red/visible region of the spectrum.

2. Cloud Free Regions

Remote sensing techniques for the three input variables (SST, τ, W) all require cloud free atmospheres. Consequently the first criteria applied to daytime passes was the presence of substantially clear areas over the VOCAR region. Nevertheless, this was not sufficient to ensure convergence in many cases. Chapter V includes a discussion of the factors thought to be responsible for this anomaly.

3. Sunlint

Having selected passes with clear regions it was necessary to assess the level of sunlint in those areas. This was done by examining the Channel 1 (percent albedo) values.

4. Match with Initial Assumptions

Once passes with clear regions, devoid of sunlint, had been selected we examined the extent to which each matched our initial assumptions. The importance of this match was reduced (somewhat) by our ability to vary the

percentage of total atmospheric water vapor confined to the MABL for iteration.

5. Gradients Observed in Satellite Images

Having generated images representing the brightness temperature difference between CH4 and CH5 (roughly indicative of atmospheric water vapor) these were examined for areas of significant moisture gradients. A great deal of small scale (10's of km) moisture variability was evident in a number of such images; these were the first cases to which the technique was applied.

6. Spatial and Temporal Considerations

Several investigators have pointed out that spatial and temporal deviations between satellite derived and radiosonde generated profiles contribute to method error. As a final selection criterion, passes which had at least five radiosonde launch stations in clear areas of the image and a time difference between pass and launch not to exceed one hour, were selected.

V. RESULTS OF SATELLITE ANALYSIS

A. APPROACH

The selected strategy was to allow the satellite data to determine cases for study. That is, initial steps were to examine the satellite images for significant patterns or gradients and then check to see if these patterns were also present in the in-situ data. This was done to provide a level of confidence in the satellite data analysis. Errors in the satellite derived boundary layer (BL) height and surface relative humidity (RH(0)) estimates result primarily from inaccuracies in the remote measurement of the input variables: 1) sea surface temperature (SST), 2) optical depth (τ), and 3) total atmospheric water vapor (W) (Kren 1987). A second source of error is deviation of the atmosphere from the assumed MABL characteristics required by the technique.

B. MABL CHARACTERISTICS FOR VOCAR

The R/V Pt. Sur sounding data was used to determine the thermal and moisture characteristics in and above the MABL for the VOCAR period. The R/V Pt. Sur profiles provide MABL measurements free from land influences. Figures 11 (a) and (b) show time series of potential temperature (K) and mixing ratio (g/kg) respectively at Pt. Sur from (00z) 27 August 93

to (06z) 29 August 93. The vertical axis is height in meters. The times representing the two selected satellite passes are indicated by black arrows along the horizontal axis. An examination of these time series shows:

- The boundary layer is well-mixed, with respect to these variables, throughout the period, as required by our initial assumptions; note the near constant values of potential temperature and mixing ratio in the MABL,
- The top of the BL is well defined by a large vertical gradient in both variables; the top of the BL is at the bottom of this gradient,
- The variables are in excellent agreement as to the boundary layer height,
- A thickening of the boundary layer occurs, in the early morning hours of 28 August; this is nearly the same time the refractive regime (as monitored at the Pt. Sur) shifted from surface based to an elevated duct.

One of the technique assumptions of Kren (1987) and Smolinski (1988) was violated throughout the entire VOCAR period; total atmospheric water vapor (W) was not confined to the MABL. Figure 12 shows a reasonably typical Pt. Sur sounding when approximately 10% of (W) was contained in the MABL. There are significant mixing ratio values above the MABL in Figure 11(b) as well. This, of course, is contrary to the assumptions. To address this departure from assumed conditions the following procedures were utilized:

- The boundary layer height algorithm was made interactive to allow the operator to select the fraction of total atmospheric water vapor (W) confined to the MABL for purposes of iteration.

- An algorithm was used to estimate the proper fraction for program entry. This algorithm vertically integrated absolute humidity (g/kg), from radiosonde measurements, and determined the portion confined to a specified BL height,
- The specified BL height was taken off the synoptic radiosonde launch from the Pt. Sur; where (both) a large increase in potential temperature and / or a large decrease in relative humidity was observed.
- The fraction of W was varied slightly (as necessary), to improve the agreement between satellite-derived and radiosonde observed boundary layer heights at the offshore stations, those considered to most closely represent the actual height of the MABL.

C. CASE STUDIES

Based on criteria previously described, two specific satellite passes were selected for intensive examination. The first, 27 August 93, represents a morning satellite pass (1605z) during a surface-based ducting regime. The second, 28 August 93, involves an afternoon pass with an elevated ducting regime. A detailed comparison of satellite-derived and in-situ observed variables is given in the following section.

1. Case One: 27 August, 1993

a. *Visible and Infrared Satellite Images*

An examination of the AVHRR Channel 1 visible image for the pass, Figure 13, shows a fairly uniform stratocumulus deck along the offshore edge of the VOCAR region. All of the sounding stations, with the exception of

NAS North Island (NZY), are in the clear. Some convective activity is located west of NZY, as is some dense cloud cover to the south. For reference, sounding stations and NOAA buoy locations are labelled on Figure 13.

The sea surface is not black between NZY and CPN as we might expect in clear areas of a Channel 1 image. Haze, resulting from variations of moisture and aerosols in the MABL that influence the optical depth; is believed responsible for this. Wake-effects in the imaging downstream of San Clemente (NUC) and Santa Catalina islands are consistent with the west-by-southwesterly winds reported just prior to the pass. The eddy-like cloud feature just offshore of Point Vicente (PVN) did not persist until the next available satellite image at 2300z.

The AVHRR Channel 4 infrared image, Figure 14, indicates the warmest regions over land as we might expect for a daytime pass; these areas are imaged white. The convective activity offshore of NZY is the coldest, followed by the heavy cloud cover along the western border of the region; these areas show as relatively dark areas on the image. The VOCAR stratocumulus cloud areas show some warmer cloud tops only slightly cooler ($1 - 2^{\circ}\text{C}$) than the ocean surface. There is some indication of SST gradients in the clear regions just offshore.

b. Sea Surface Temperature Image

In displaying the sea surface temperature, Figure 15, clouds and cloud contaminated pixels were imaged black. The cooler temperatures are light blue (primarily offshore) warming to a purple shade as we approach the shoreline to the east, and the warmest areas, (red areas other than that in the lee of PVN) are primarily between PVN and NZY. In the clear-sky regions numerous sea surface temperature gradients are apparent. We expect to see changes in the height of the boundary layer in the vicinity of these gradients. We also expect the greatest boundary layer heights over the region of maximum SST.

There are two locations where the cloud screening system fails to detect the presence of clouds. The first is that eddy-like cloud feature west of PVN; the second is a small, light cloud midway between CPN and Santa Catalina Island to the west. A comparison of the visible image, Figure 13, with the image of SST, Figure 15, shows that both features were not blacked-out; probably a function of their low/thin/relatively-warm nature.

c. Boundary Layer Height Image

The boundary layer height image from the algorithm, Figure 16, shows a great deal of structure over the region. The actual radiosonde computed boundary layer height at each launch station is displayed on the image for

comparison. There is an obvious slope to the boundary layer; sloping downward from a high point near CPN to the west as well as the northwest. As expected, the largest boundary layer height gradients are collocated with those of SST and the greatest heights are in the area of maximum SST; a function of increased convective mixing.

The western portion of the image is black. These areas are either cloud-covered or also possibly areas where the model would not converge. Non-convergence indicates that the computed value of one of the input variables is inconsistent with the other two.

d. Transects of Satellite BL Heights

In order to further quantify the variability, and in an attempt to explore possible relationships between the boundary layer and refractivity, we will examine boundary layer height transects as follows:

- The **Coastal Transect**, VBG / NTD / PVN / CPN / NZY - from Vandenburg past Pt. Mugu, Pt. Vicente and Camp Pendleton, ending at San Diego.
- The **Offshore Transect**, VBG / NSI / NUC / NZY - from Vandenburg past San Nicolas and San Clemente Islands, ending at San Diego.
- The **VOCAR Transect**, NTD / PSUR / NUC / NZY - from Pt. Mugu past the Pt. Sur and San Clemente Island to San Diego.

These transects were illustrated on Figure 3; all transects were run from west to east to match the

orientation of the image. The last route encompasses both legs of the range along which refractive effects (received signal strength) were monitored during the VOCAR IOP. Any gaps in these figures correspond to areas covered by clouds or model non-convergence. Seeing the gaps in our satellite boundary layer heights (resulting from cloud cover) caused us to ask the following question: Can we fill in these data gaps by applying the IR Duct Technique, Rosenthal and Helvey (1992), which applies to cloud covered regions?

Our approach did not follow exactly Rosenthal and Helvey's guidelines for application of the method; however, it was similar enough to draw some preliminary conclusions. Instead of using climatological SST's to determine $T(\text{cloud}) - T(\text{sea}) = [\text{delta}T]$, we used satellite SST's from clear-sky areas in the vicinity of the clouds in question. This $[\text{delta}T]$ became the entering argument for the inversion base-height temperature relationship. The requirement for minimal upper tropospheric moisture was not met. In addition, our IR cloud top temperature sampling scheme averaged nine (3×3) pixel values. Because of the patchy nature of the cloudy areas we examined, there is a possibility that SST's (viewed in the holes among the clouds) contaminated cloud top temperatures.

This approach, based on SST's from clear-sky areas, was applied to the cloudy areas along our transects at approximately 30-40 km intervals. The results are

overlayed upon our satellite boundary layer height transects and appear as dashed black lines in the areas lacking satellite data.

(1) *The Coastal Transect:* Figure 17 is boundary layer heights along the coast from VBG to NZY. We did not have a sounding at PVN at this time. The cross section shows the general slope of the boundary layer downward from southeast to northwest. The boxes overlaying the curve indicate the extent of the elevated trapping layer inferred from an M-index profile measured by radiosonde at each of the stations. There is excellent agreement between the bottom of the trapping layer and the top of the boundary layer at all stations with the exception of NZY. It is believed this is due to the cloud cover at that location. Furthermore, the slope of the satellite-derived boundary layer agrees well with that of the trapping layer. East of VBG, an area of non-convergence due to clouds, is matched well with the heights obtained via the IR Duct Technique, as indicated by the dashed black line.

Figures 18 (a) and (b) are vertical cross sections of observed potential temperature and mixing ratio along the coastal transect. Both the 295 (K) isotherm and the 11 (g/kg) isopleth correspond to the top of the well-mixed layer. The boundary layer slope (downward from east to west) agrees well with the slope of the satellite curve.

The eastern NZY sounding does depart from the upward west-east slope of the top of the MABL. This sounding has weaker low level stability and convective cloudiness in the region.

(2) *The Offshore Transect:* Figure 19 is boundary layer height along the offshore transect from VBG past NSI and NUC to NZY. This cross section also shows the general slope downward from east to west. There is good agreement between the bottom of the inferred trapping layer (boxes overlaying the curve) and the height of the MABL, except at NUC and in particular at NZY. Both of these locations have cloud cover in the vicinity of the station. Nevertheless, the slope of the layers agrees quite well. The cloud-covered area just east of VBG again agrees well with an application of the IR Duct Technique. The area between NSI and NUC varies over 100 meters in the range of the satellite MABL heights. See Table V(a) for specific values.

(3) *The VOCAR Transect:* Figure 20 is boundary layer height along the VOCAR transect from NTD, past PSUR and NUC to NZY. The slope downward from east to west is confirmed. Although the match between boundary layer height and location of the bottom of the trapping layer is reduced, the slope of the layers is substantially similar. Once again those stations experiencing nearby

cloud cover are least likely to agree. The IR Duct Technique satisfactorily assigns height values to the cloud-covered portion of the transect between PSUR and NUC.

These satellite-derived figures indicate potential temporal and spatial variability of BL heights and refractive conditions in the clear areas of the VOCAR region during this period. That premise will be further examined in the next section, using in-situ data.

e. M-Index Profiles

In Figures 21(a) and (b) are M-index profiles from consecutive ascent / descent soundings at the Pt. Sur on 27 August. Those shown are up to 6 hours prior to our selected satellite pass. The ascent / descent soundings were achieved by having a release mechanism attached to the radiosonde to allow it to descend after reaching approximately 700 mb. This provided a second realization of MABL characteristics nearby the original launch point after a short time interval. Location of the trapping layers, where $dM/dz < 0$, are indicated in the figures. We can assume the radiosonde did not descend along the same path it ascended. Furthermore, the two trips are usually separated by 1-1.5 hours in time. Comparisons of the ascent and descent profiles indicate the spatial and temporal variability of refractive conditions in the vicinity of Pt. Sur, during the VOCAR IOP.

Specifically, Figure 21(a), ascent at 1042z, shows a primary (inversion-based) layer from about 70 - 185 meters, along with numerous small elevated layers above. Figure 21(a), descent at 1123z, has it's primary layer from 110 - 210 meters with a secondary from 275 - 310 m. In addition there are two other elevated layers present. Figure 21(b), ascent at 1432z, shows a primary layer from 220 - 325 meters with secondaries from 480 - 500 and 570 - 605 m. Figure 21(b), descent at 1517z, has a primary at 225 - 360 m and another at 470 - 490 m. If we examine the transition from ascent to descent conditions (in both cases) - the upward shift in the bottom of the primary layer indicates entrainment from below exceeds subsidence from above. We might reasonably assume this variability applies to the entire VOCAR region, and suggests 50 meter changes in the trapping layers are common. Unfortunately, not all sounding stations conducted up / down launches.

An important point is that many of the M-index profiles indicate the existence of multiple elevated trapping layers. The satellite technique being described is directed at the MABL structure and is unable to address these additional layers. It can only resolve the bottom of the inferred trapping layer associated with the inversion at the top of the MABL. However, this is often the deepest and most important layer.

f. Surface Relative Humidity Image

Figure 22 shows satellite derived surface relative humidity, $RH(0)$, from the algorithm, over the region. Solid clouds are imaged black; the white areas are where $RH(0)$ exceeds 97% regardless of the presence or absence of clouds. Most of the offshore region is cloudy or has greater than 97% $RH(0)$. Drier surface conditions are found along the coast from west of NTD to the Los Angeles basin and in the lee of the islands (wake effects). The important aspect of this image is the dry region (minimum in $RH(0)$) between PVN and NZY. This is coincident with the region of maximum boundary layer heights. The model is attempting to distribute the available moisture through a deeper layer, which is to be expected. Data to confirm this analysis are not available except for the R/V Pt. Sur. However, the moisture patterns are consistent for the real wind conditions.

An interesting point arises when the $RH(0)$ image is compared with the visible and BL height images. What is observed are clouds in the $RH(0)$ image that are not removed by the current cloud screening system. These are generally low, relatively warm sections near the edges of the cloudy areas. The surface relative humidity values, resulting from the algorithm, are quite high (95-97%), as we would expect in a region of low clouds but the BL height values often do not converge. This is not necessarily a deficiency, but is

the result of applying convergence criteria to BL heights and not to surface relative humidity values. It is believed that the value of one of the input variables is impacted by cloud contamination which causes it to be inconsistent with the others.

2. Case Two: 28 August, 1993

The satellite pass selected for this case was at (2322z). This pass comes 31 hours after the previous pass and approximately 11 hours after the boundary layer had thickened as shown in Figure 11.

a. Visible and Infrared Satellite Images

The AVHRR Channel 1 visible image, shown in Figure 24, reveals a fairly uniform stratocumulus deck over the western half of the region. Five of the eight sounding locations are in the clear sky region, but NTD, PSUR, and NUC are not. There are clear areas in the vicinity of these three stations that are used for satellite-derived boundary layer height comparisons. Apparently the boundary layer is low enough over San Nicolas (NSI) and San Clemente (NUC) islands to be influenced by the topography so that obvious 'wake-effects' are present. The cloud plumes in the lee of both islands have a distinct satellite signature. The highest points on these two islands are 283 and 615 m respectively. The pattern is consistent with the westerly winds reported about this time.

The AVHRR Channel 4 infrared image in Figure 25 shows the warmest areas over the land regions which are imaged white. The convective activity inland (NE) of PVN shows the coldest cloud-tops, which are imaged black. For the low cloud areas, the coldest cloud-tops are those west of VBG, followed by the region between NSI and NUC, all of which are dark grey areas in this thermal image. Some indication of SST gradients appears in the clear-sky regions just offshore.

b. Sea Surface Temperature Image

The sea surface temperature image in Figure 26 also has its coolest areas offshore (light-blue) warming toward the coast to the east. The largest SST gradients and maximum values are located in the region between PVN and NZY, as was the case the day before. However, the average temperature in this region is higher than the previous day and this is to be expected, local time for this image is 1622, as opposed to 0905 on 27 August. This image was enhanced to emphasize SST in the clear-sky areas (clouds and cloud-contaminated pixels are black) but valid temperatures are available in the 'holes' within portions of the stratocumulus deck. Again our cloud screening system appears deficient in two locations: 1) west and southwest of NTD, and 2) west and southwest of NZY. These clouds are

low, thin with warm tops. The SST details in these regions are affected by the clouds.

c. Boundary Layer Height Image

The boundary layer height image, Figure 27, shows a great deal of structure throughout. The actual radiosonde computed boundary layer height at each launch station is displayed on the image for comparison. The MABL has deepened in the previous 24 hours at all VOCAR measurement sites. The slope of the boundary layer is similar to the day before; sloping downward from a high point near CPN to the west as well as the northwest.

The largest boundary layer height gradients are collocated with the largest SST gradients. The greatest heights are in the area of maximum SST; another indication of increased convective mixing. The black regions in the western portion of the image are cloud covered. There are numerous reasonable height values among the open cells in the stratocumulus deck offshore.

d. Transects of Satellite BL Heights

Vertical transects of boundary layer height were obtained along the same paths as those from 27 August. These were:

- The *Coastal Transect*, VBG / NTD / PVN / CPN / NZY,
- The *Offshore Transect*, VBG / NSI / NUC / NZY, and
- The *VOCAR Transect*, NTD / PSUR / NUC / NZY.

(1) *The Coastal Transect:* Figure 28 shows boundary layer height along the coast from VBG to NZY. The general downward slope from east to west is apparent again. Agreement between satellite boundary layer heights and the bottom of the trapping layer is good. The slope of the satellite boundary layer agrees with that of the radiosonde trapping layer. The MABL is at a maximum between PVN / CPN and appears to be highly variable in this region. In this particular case, we are missing synoptic soundings for both PVN and CPN. However, we have soundings for both locations, before and after the pass. At PVN the 20z sounding shows a primary (inversion-based) trapping layer from 460 - 635m. After the pass, at 04z (29 August) the trapping layer has narrowed to 425 - 560m. Because these layers are so similar, an average of these two values was plotted on Figure 28 and is considered representative. At CPN the 20z sounding has a primary trapping layer from 350 - 460m. The 04z sounding shows a primary trapping layer from 430 - 540m. This sounding provides best agreement with satellite heights and was, therefore, selected. This case illustrates the difficulties arising when comparing overland soundings with our overwater satellite-derived BL heights.

(2) *The Offshore Transect:* Figure 29 shows boundary layer height along the offshore transect from VBG past NSI and NUC to NZY. Due to clouds in this region of

the pass there are substantial areas missing satellite data. However, where satellite data does exist the agreement with trapping layer heights is quite good; the slope of the two layers is in excellent agreement. The IR Duct Technique was used to obtain quite reliable information immediately east of VBG. However, the technique wasn't nearly as successful in the other two regions lacking satellite data.

Figures 30 (a) and (b) show cross sections of radiosonde observed potential temperature and mixing ratio along the path corresponding to the offshore transect. Both the 293(K) isotherm and the 9(g/kg) isopleth correspond to the top of the well-mixed layer. Comparison with Figure 29 indicates fair agreement on the slope of the MABL with the satellite curve. The major deficiency is in the vicinity of VBG where the satellite MABL height is lower than the raob.

(3) *The VOCAR Transect:* Figure 31 shows boundary layer height along the VOCAR transect from NTD past PSUR and NUC to NZY. The satellite indicates a weak downward BL slope from east to west. Good agreement is shown between observed and satellite-derived heights and slopes. Once again the missing data is the result of clouds, this does not prevent performing comparisons. The IR Duct Technique does yield reliable values in this situation. As was the case on 27 August, these figures

support the suggestion of extensive variability of BL heights and refractive conditions in the clear areas of the VOCAR region during the period.

e. M-Index Profiles

Figures 32(a) and (b) show M-index profiles from consecutive ascent / descent soundings at the Pt. Sur. Figure 32(a) represents conditions 8 hours prior to our satellite pass, Figure 32(b) shows conditions 3.5 hours after the pass. Location of the trapping layers, where $dM/dz < 0$, are indicated in the figures. The temporal and spatial variability of refractive conditions is evident from comparisons of ascent and descent profiles. Specifically, Figure 32(a), ascent at 1502z, shows a primary (inversion-based) trapping layer from 430 - 510 meters and a secondary layer from 620 - 645m. The descent at 1519z, only captured one layer from 400 - 430m. There are, again, multiple trapping layers in the vicinity of the Pt. Sur. This satellite technique is currently unable to address these layers.

Figure 32(b), ascent at 0242z, shows a primary trapping layer from 365 - 425m with a secondary from 690 - 745m. The descent at 0320z shows three trapping layers: 330 - 430m, 470 - 530m, and 815 - 880m. For this day, if we examine the transition from ascent to descent conditions (in both cases) the downward shift in the base of the primary

trapping layer is indicative of subsidence from above exceeding entrainment from below. Similar to the case on 27 August, the satellite information indicates this variability over to the rest of the region.

f. Surface Relative Humidity Image

Figure 33 is satellite derived surface relative humidity, $RH(0)$, from the algorithm, over the region. Solid clouds are imaged black; the white portions are regions where $RH(0)$ exceeds 97% regardless of the presence or absence of clouds. Much of the offshore region is cloudy or has greater than 97% $RH(0)$. Drier regions follow the coastline from Pt. Mugu to San Diego. Once again our attention is drawn to the substantially dry region between PVN and NZY, similar to that seen on 27 August. As was the case the day before this local minimum is collocated with the maximum in boundary layer height. Once again the model is distributing moisture over a deeper layer. Wake effects are again observed downstream of San Clemente (NUC) and Santa Catalina islands consistent with the winds shown in Figure 34, lending some measure of confidence to our satellite interpretation.

D. METHOD VERIFICATION

The relative accuracies of the satellite derived data were evaluated. In this regard, Smolinski (1988) conducted a sensitivity study to assess the effect of combined

measurement errors under several different (simulated) boundary layers. The standard deviations for surface relative humidity $RH(0)$ ranged from 2.1 - 6.3%. The standard deviations for boundary layer height ranged from 95 to 169 m. Errors in both estimates tended to increase as $RH(0)$ decreased. There was little change in the estimates as a result of changes in sea surface temperature. He concluded that total atmospheric water vapor was the most important input variable, followed by optical depth and SST.

The remainder of this section discusses each of these verification efforts.

1. Sea Surface Temperature

Satellite-derived SST's using the NOAA/NESDIS daytime split NLSST algorithm were compared with those from the 5 NOAA buoys and 1 observation from the Pt. Sur. This is the current algorithm in operational use at NOAA, with advertised (global-scale) accuracy of about 0.5°C . The accuracy of this estimate is important as a bottom boundary condition for the iterative scheme. The average error was 0.63°C . Table 2 contains the results of the SST comparisons.

2. Boundary Layer Height

We brought satellite-derived boundary layer height into agreement with offshore radiosonde measurements, PSUR, NSI, and NUC by varying the amount of total water vapor

confined to the MABL. Having attained the best possible fit we compared the agreement, at all 8 stations, both days. The average error for this comparison was 58.5m.

For the 28 August pass, the best agreement with observed boundary layer heights was obtained by using 29% total atmospheric water vapor confined to the MABL. Compared to the previous day, this value closely agrees with the value (30%) indicated by our vertical moisture integration program. The errors range from 5 to 210 m, the average error for the offshore stations is 31 m. The greatest error occurs at CPN which is near the maximum in boundary layer height. The MABL at this location is undoubtedly influenced by surface heating along the coast.

For the 27 August pass, the best agreement with observed boundary layer heights was achieved with 27.5% total atmospheric water vapor confined to the MABL. This disagrees with our vertical moisture integration program that estimated only 12% was present in the MABL. The reason for this difference is still unclear. The errors range from 41 to 113 m, the average error for the three offshore stations is 57 m. Table 3 shows the results of the BL height comparisons.

3. Surface Relative Humidity, RH(0)

The iteratively derived surface relative humidity was compared to observed values at the Pt. Sur. It was

decided that Pt. Sur provided the only in-situ values that truly represented a near-surface value and avoided any land influence. The average error for this comparison was 6.0 %. Table 4 contains the results of the RH(0) verification.

4. Comparison With IR Duct Technique

The dashed black lines on most of our satellite transects graphically show our attempt to compare this multispectral MABL method with the IR Duct Technique. An examination of figures 20, 22, 23, 33, and 35 shows that the two methods can agree quite well at times but diverge significantly at others. This is believed due to the cloud top temperature sampling scheme we employed. Our (3 x 3) sample average might include pixels contaminated by SST, because of the patchy nature of these clouds. The contaminated pixels would be warmer than nearby cloudy pixels. This would decrease the magnitude of $[\Delta T]$, leading to an underestimate of inversion base altitude. Examination of the BL height transects indicates a tendency toward low values.

In light of the somewhat abbreviated procedure we employed these results are, nevertheless, encouraging. It seems that an eventual integration of the two techniques holds promise for (someday) providing overall regional input to coastal range-dependent propagation models. Tables 5(a)

and (b) summarize the details of our application of the IR Duct Technique.

VI. CONCLUSIONS

The marine atmospheric boundary layer (MABL) was successfully mapped over a coastal region, using multispectral AVHRR (CH 1, 4 & 5) satellite data, acquired during the VOCAR IOP. An iterative scheme utilizing satellite-derived total atmospheric water vapor, aerosol optical depth and sea surface temperature; via the relationship between radiative extinction and relative humidity, was employed. This technique was originally proposed by Kren (1987) and later verified by Smolinski (1988). A comparison of satellite-derived and radiosonde-measured boundary layer heights and slopes showed good agreement. Further examination indicates that the method is somewhat capable of tracking the height of the bottom of a trapping layer, associated with the inversion at the top of the MABL, inferred from soundings.

Satellite images representing boundary layer height and surface relative humidity show large spatial and temporal variability over the region. In-situ observations captured similar variability in refractive conditions as well. The presence of multiple elevated trapping layers in the soundings from the Pt. Sur indicate an aspect of refractive conditions which the model is currently unable to address. An abbreviated comparison with the IR Duct Technique,

Rosenthal and Helvey, (1992) which applies to cloudy regions, indicates potential for integration with this method, which applies to clear areas.

Using a program which integrated absolute humidity to 10 km and found the fraction confined to a pre-determined BL height (taken from the synoptic Pt. Sur sounding;) the assumption of total atmospheric water vapor confined to the MABL was relaxed, and the model driven toward agreement with the observed offshore boundary layer heights. Average error for BL height estimates at the offshore locations was 58.5 m, for surface relative humidity at the Pt. Sur was 6.0 %, for sea surface temperature at the five NOAA buoys and the Pt. Sur was 0.63°C.

The largest gradients and maximum of sea surface temperature are collocated with those of boundary layer height; a result of buoyant production of turbulent kinetic energy. These areas represent the minimum in surface relative humidity, as was the case for Smolinski (1988). Since the model is attempting to distribute the available moisture through a deeper layer; this is expected.

Two primary questions which remain unanswered are: 1) why does our radiosonde estimate of total atmospheric water vapor confined to the MABL on 27 August not agree with that value which yields best agreement on boundary layer heights? 2) why did the method not converge over clear portions of

satellite images during some other periods within the VOCAR IOP?

Recommendations for further study are: 1) conduct additional verification with other VOCAR time periods, 2) merge this approach with that of the IR Duct Technique, 3) using the integrated technique (Kren-Smolinski / IR Duct) perform MABL mapping with all applicable NOAA passes during VOCAR for the entire region, 4) use the surface relative humidity results, along with other remotely sensed data, i.e. SSM/I winds, to explore satellite evaporation duct analysis.

APPENDIX

This appendix serves as a convenient location to consolidate all the figures discussed in the text of this thesis.

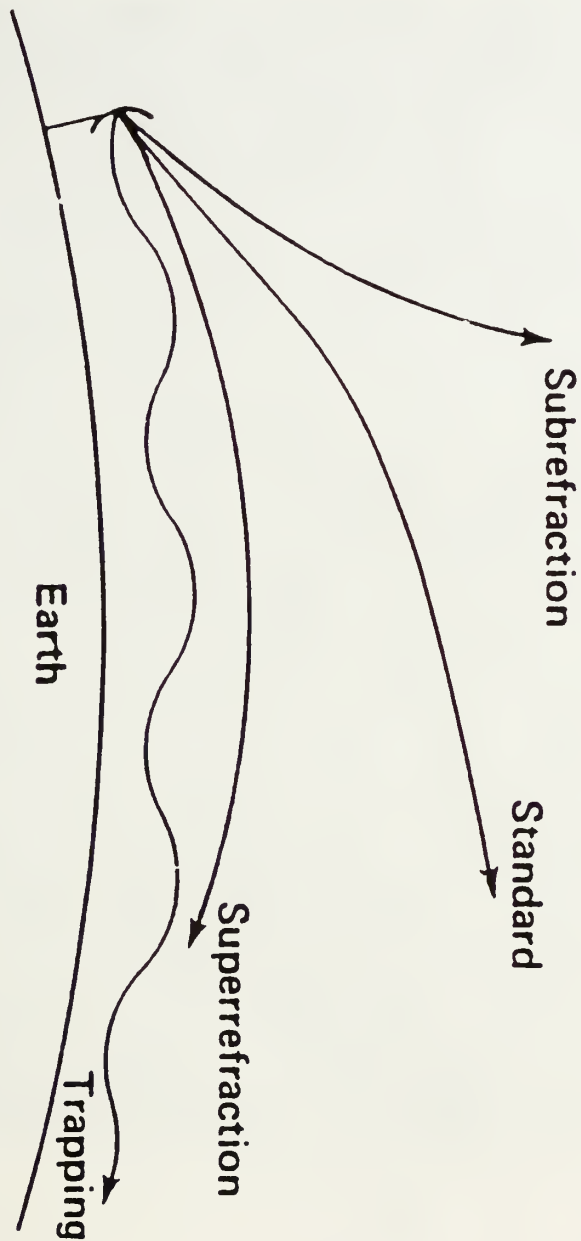


Figure 1: EM ray propagation under various refractive conditions. From Ko et al. (1983).

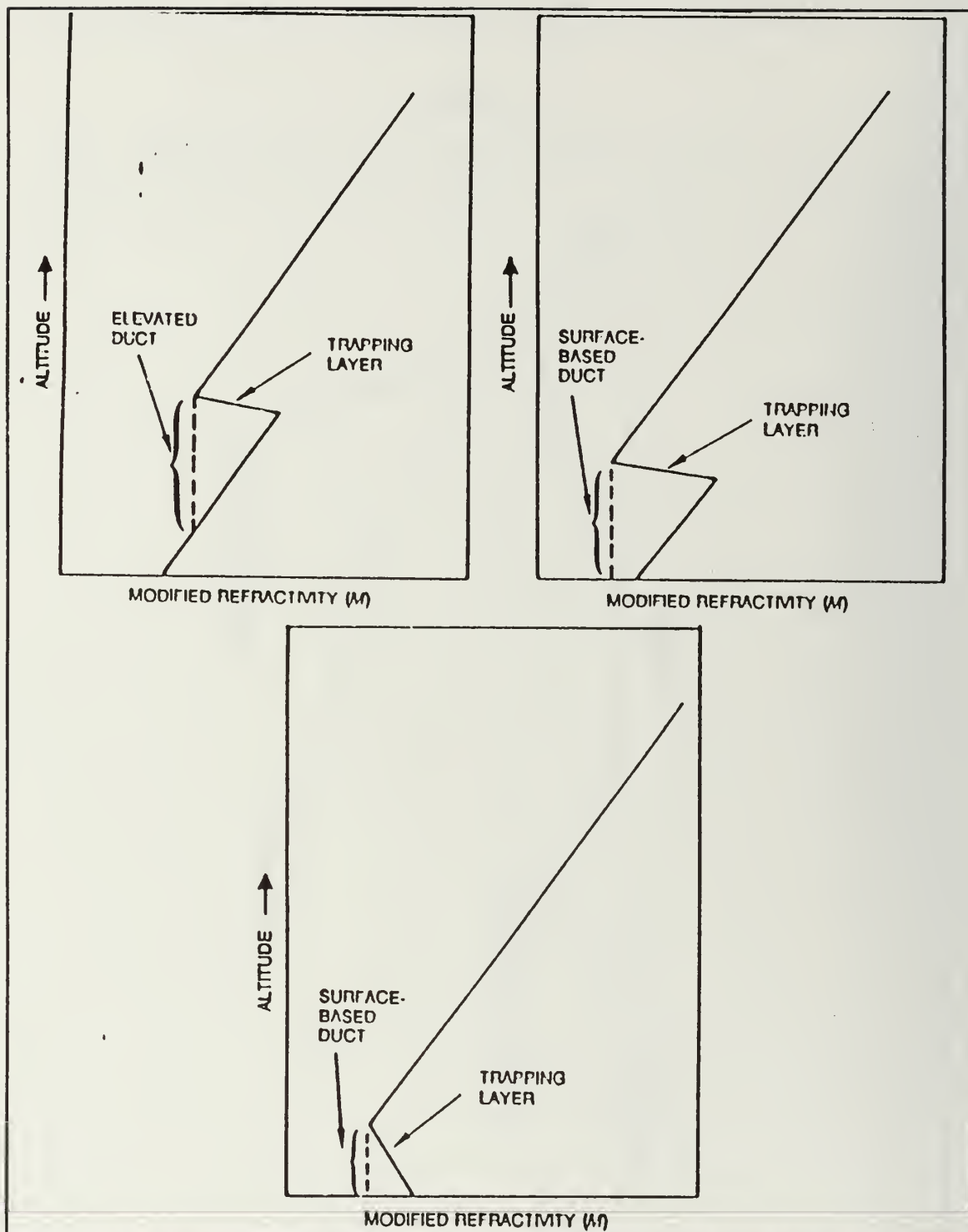


Figure 2: Examples of ducts. Fig. 2a (upper left) is an elevated duct, Fig 2b (upper right) is a surface-based duct from an elevated trapping layer, and 2c (bottom) is a surface-based duct from a surface trapping layer. From Paulus (1989).

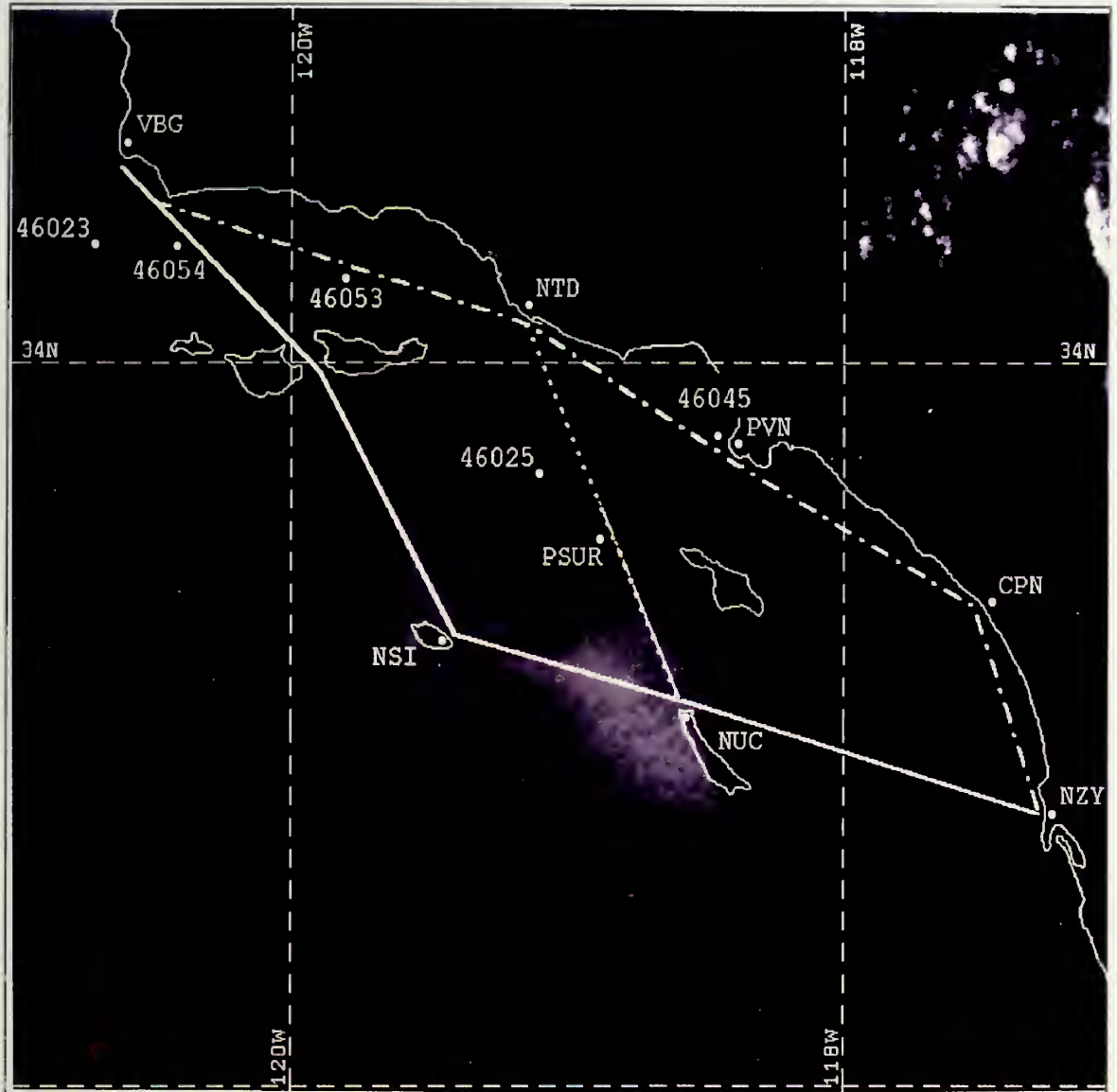


Figure 3: NOAA 11 AVHRR Channel 1 visible image of the VOCAR region at 2322z, 28 August 1993. Location of all sounding stations and NOAA buoys are shown, as are the three routes along which we will transect the satellite-derived images.

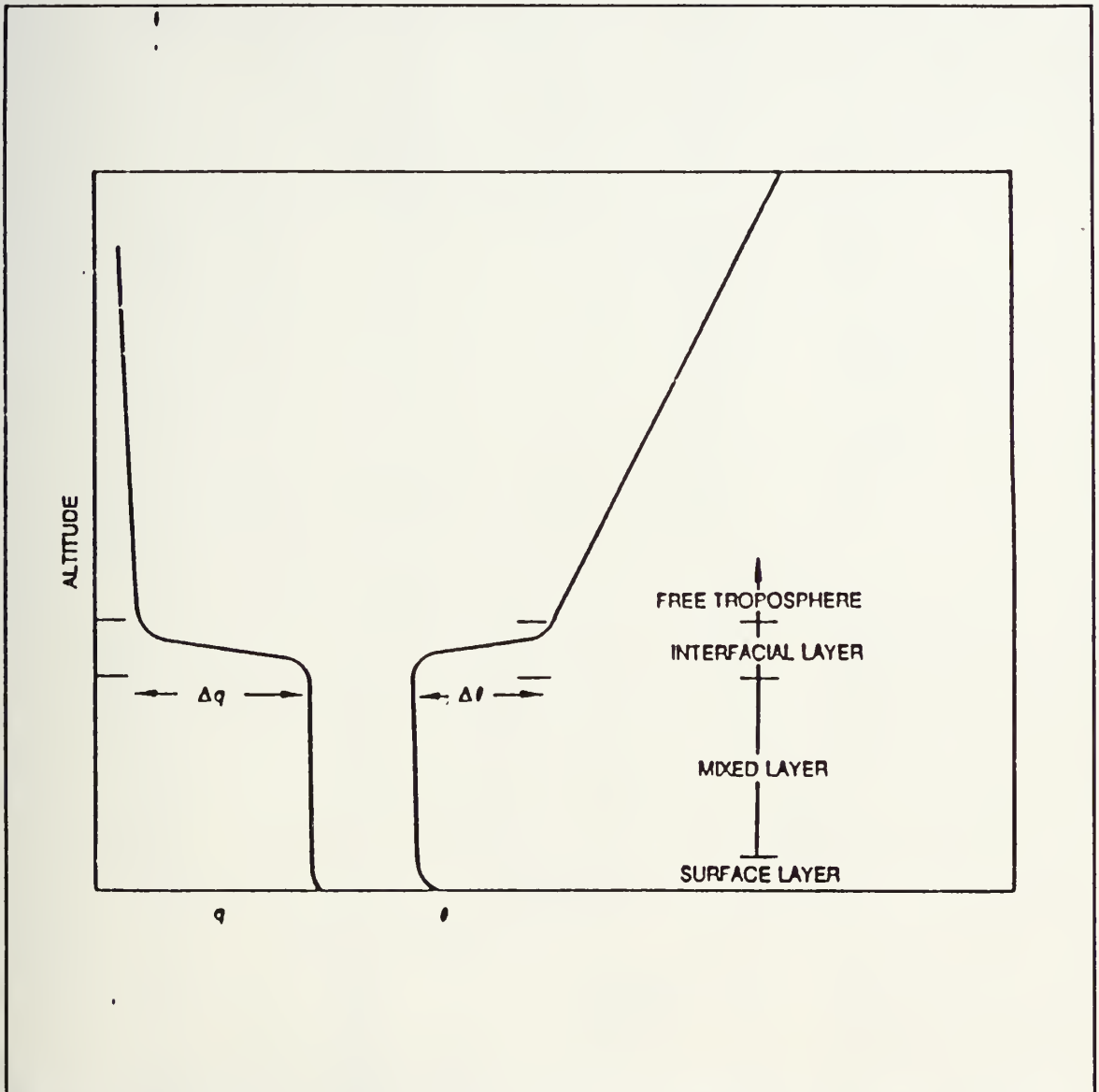
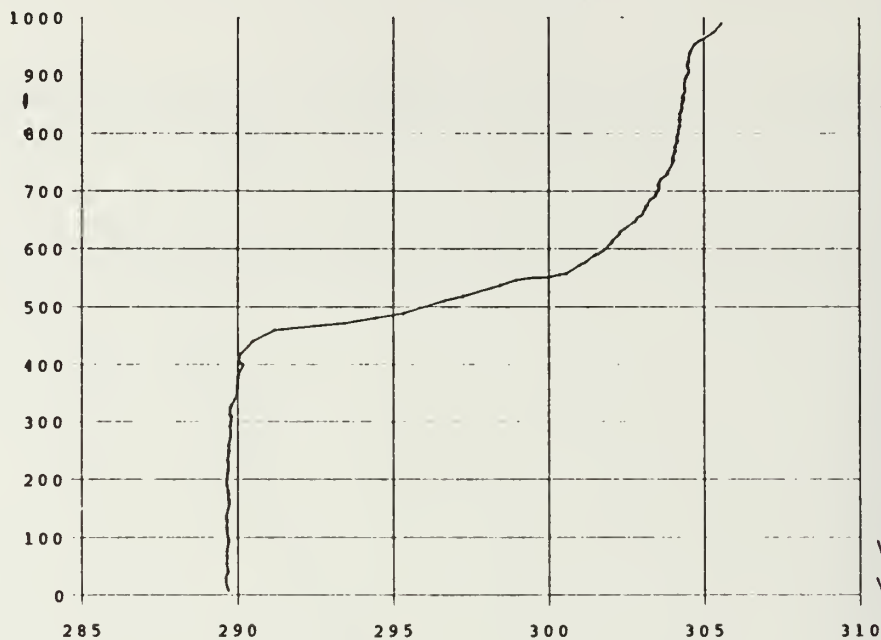


Figure 4: Marine Atmospheric Boundary Layer (MABL). MABL with negative vertical humidity gradient and positive vertical temperature gradient (inversion) in interfacial layer. From Paulus (1989).

930828/2352 0

PSUR

THTA



930828/2352 0

PSUR

MIXR



Figure 5: Pt. Sur sounding, 2352z, 28 August 1993. Fig. (a) shows mixing ratio and (b) shows potential temperature versus height (m). Note the constant values within the MABL, up to about 400m. The boundary layer is well-mixed.

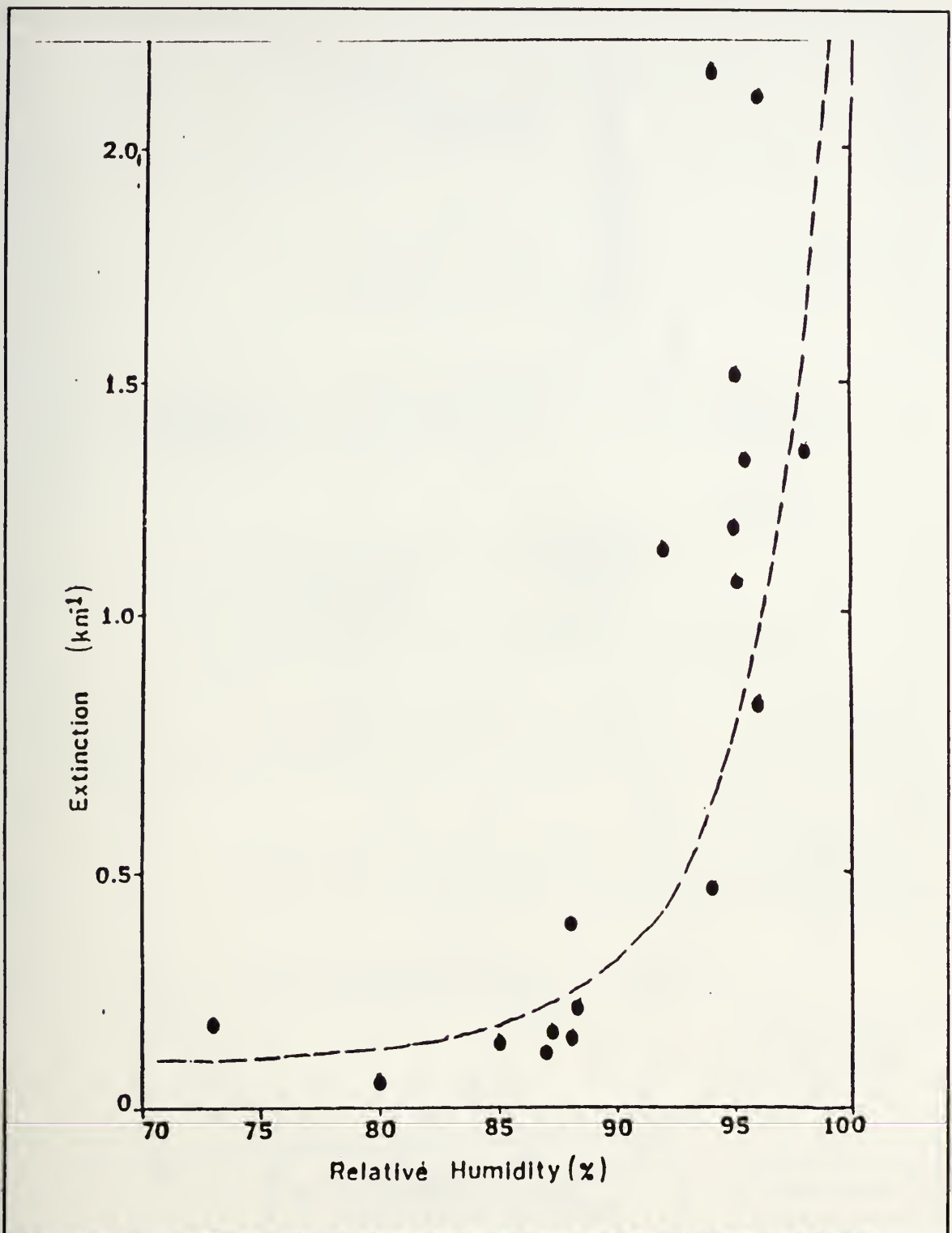
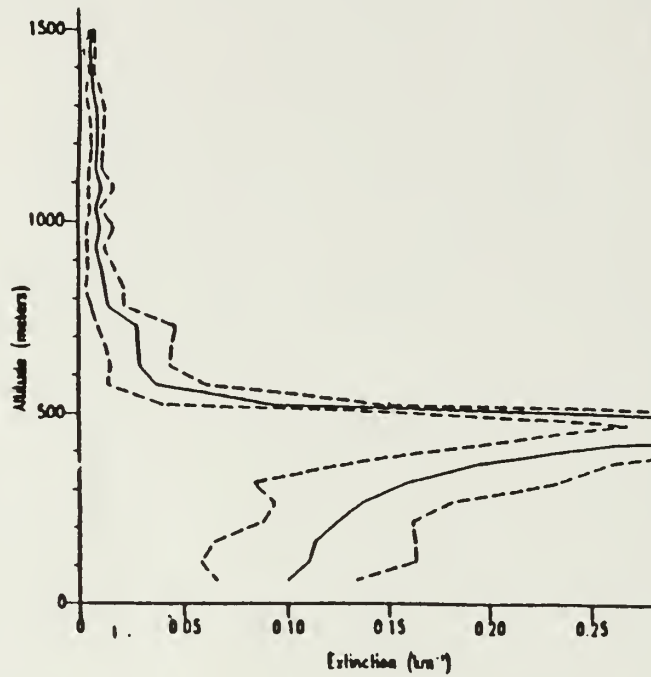


Figure 6: Value of extinction versus relative humidity based on MABL aircraft measurements from Durkee (1984). The functional relationship between these variables (Eq. 4) is also plotted.



5 October 1992

Spiral at B1

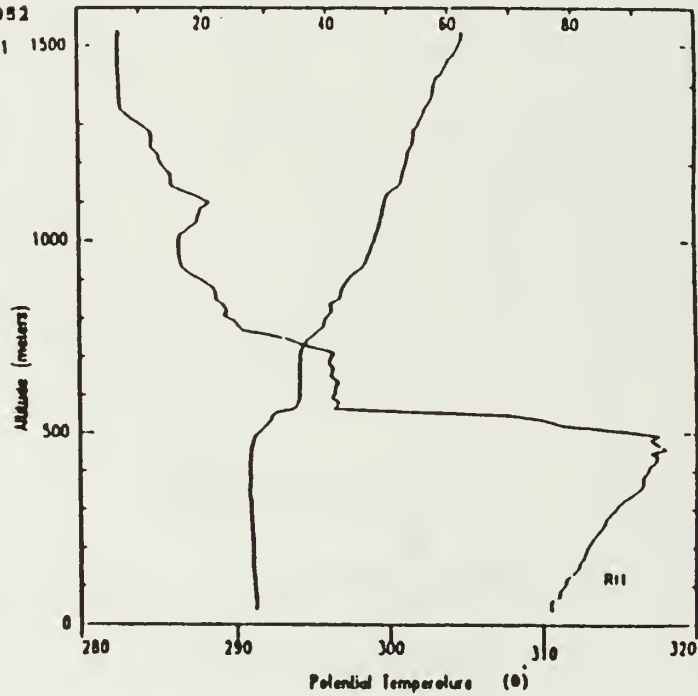


Figure 7: Profiles of extinction, potential temperature and relative humidity: Case B1 from Durkee (1984).

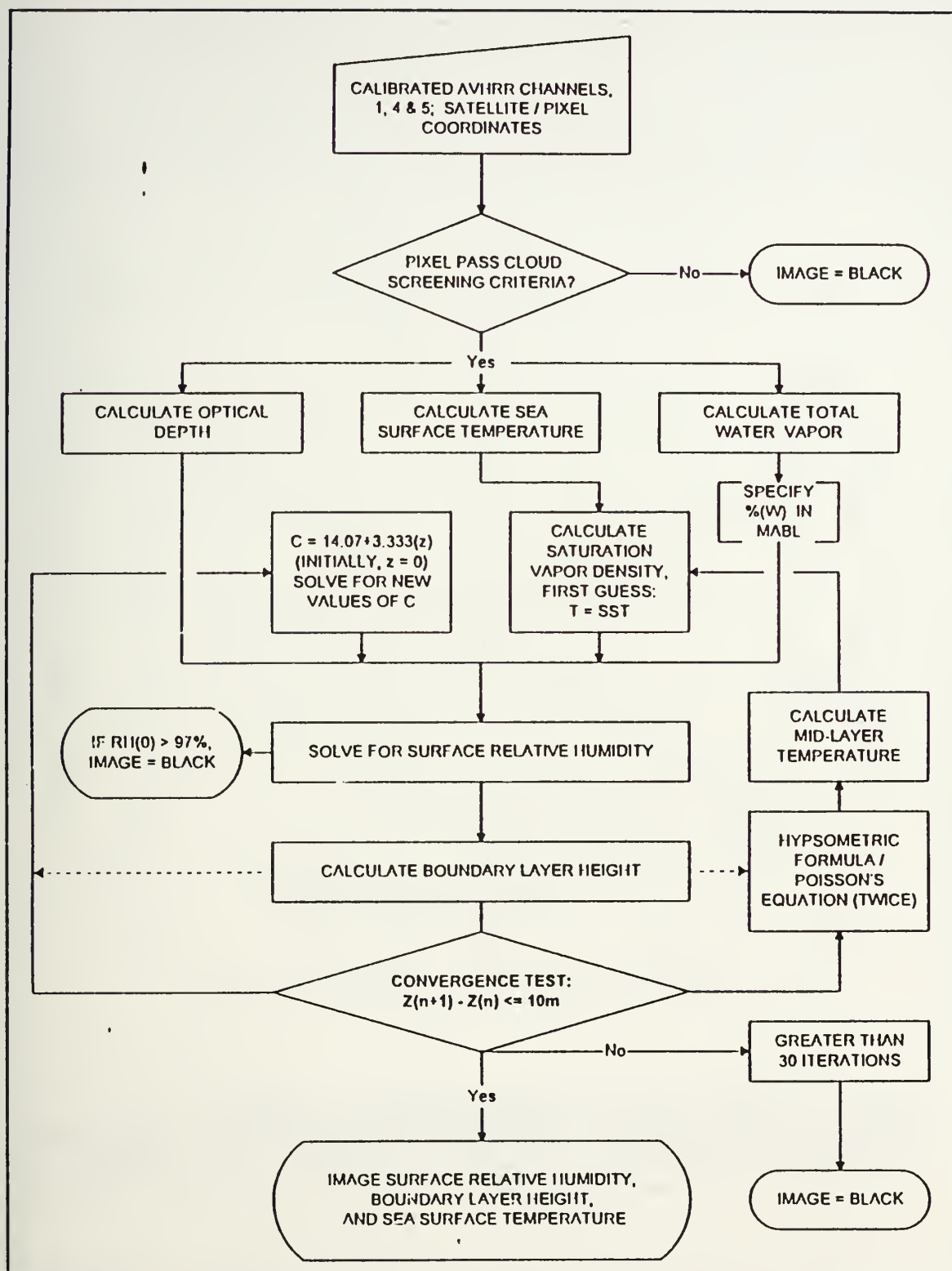


Figure 8: Sequence of events to determine surface relative humidity and boundary layer height; then to produce an image of these fields.

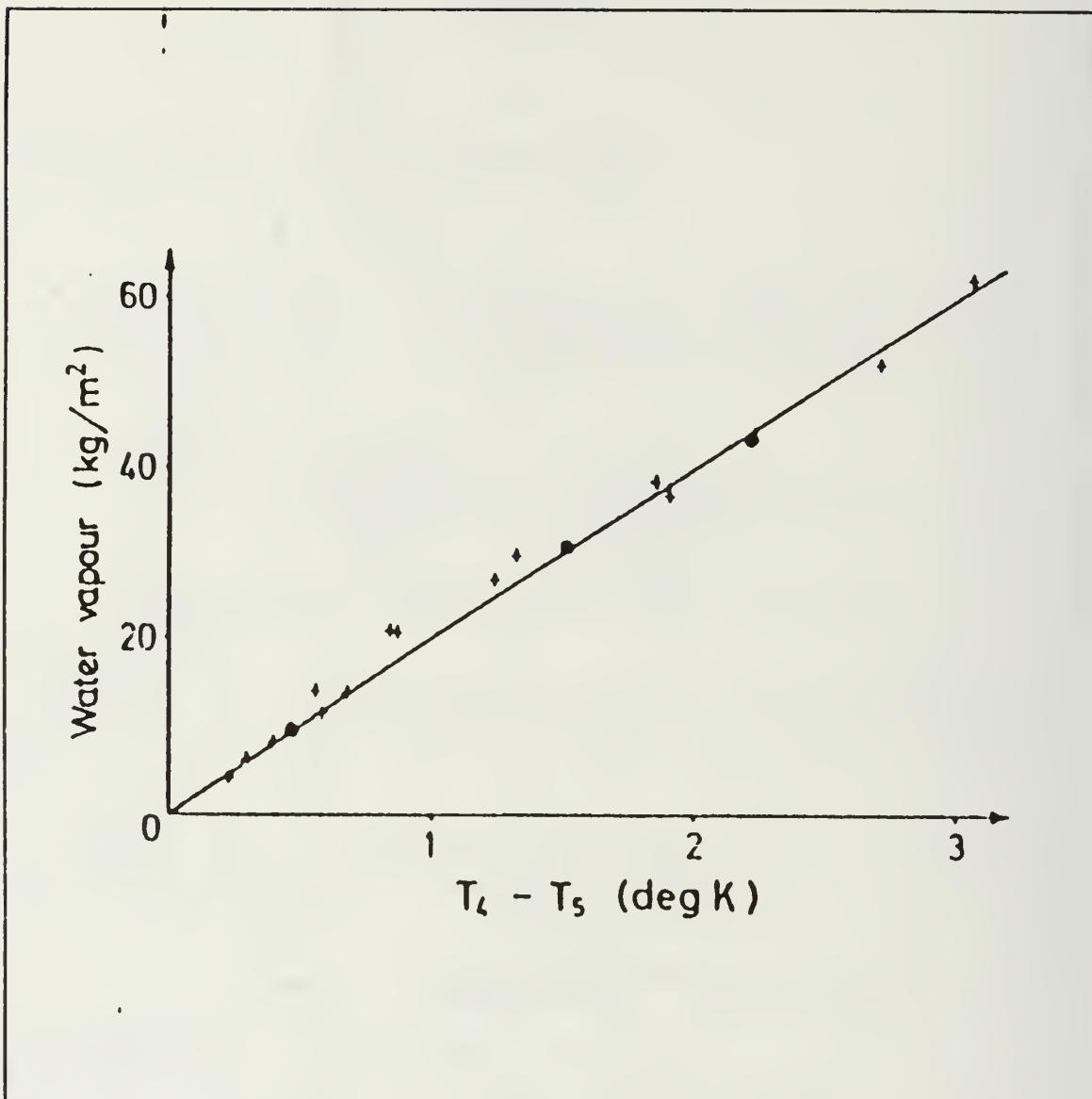


Figure 9: Total water vapor content as a function of brightness temperature difference calculated for the mean atmospheric conditions + (circled) and for the extreme atmospheric conditions (+).

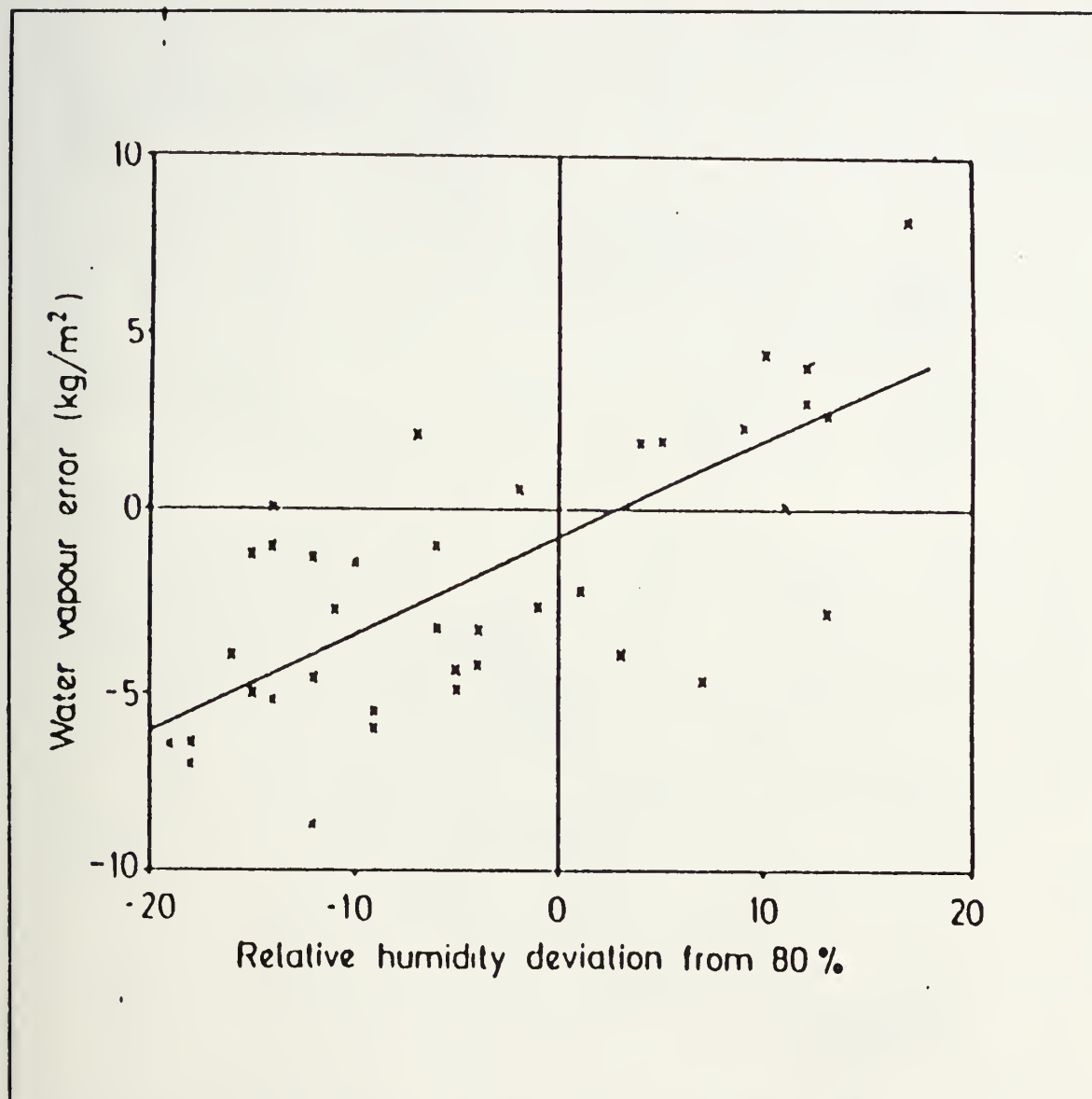


Figure 10: Difference between the ship-measured and the calculated water vapor as a function of the relative humidity deviation from the constant value 80%.

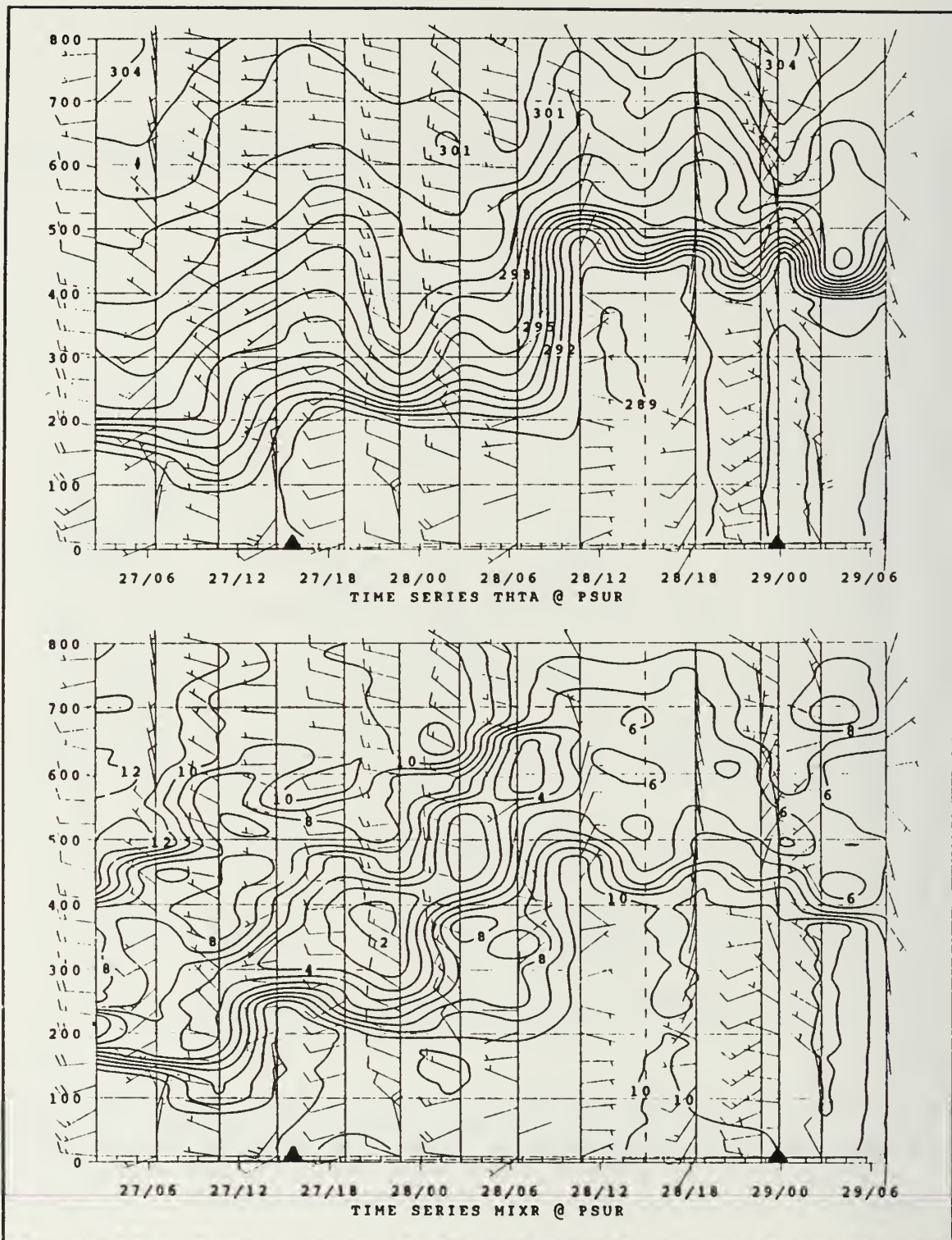


Figure 11: Time series of (a) potential temperature (K) and (b) mixing ratio (g/kg) versus height (meters) at the Pt. Sur from 00z, 27 August to 06z, 29 August 1993. Time of satellite passes indicated by black arrows on time axis.

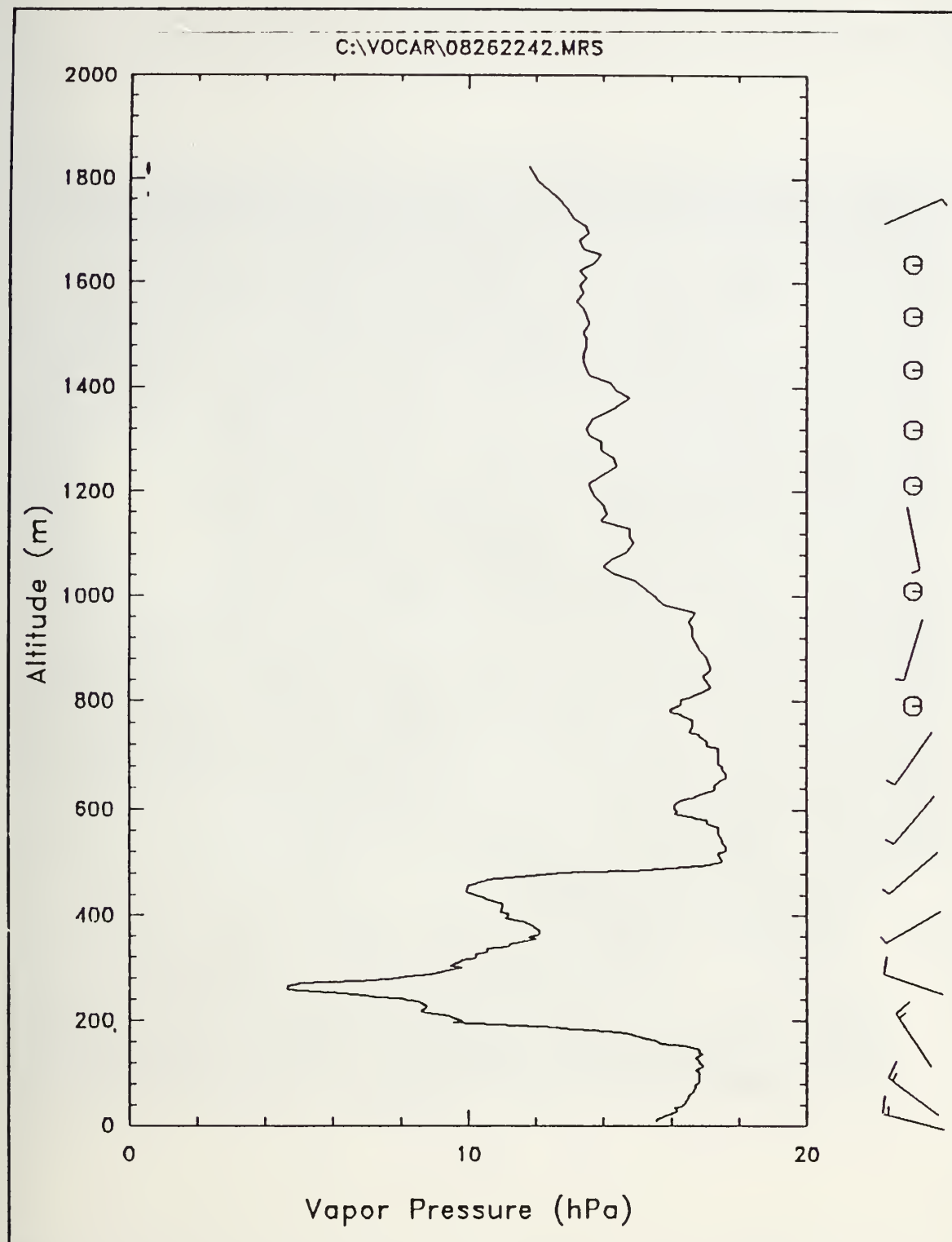


Figure 12: Pt. Sur sounding at 2242z, 26 August, 1993 showing vapor pressure (hPa) versus height in meters. Note the significant moisture above the BL, which in this case is near 200 m.

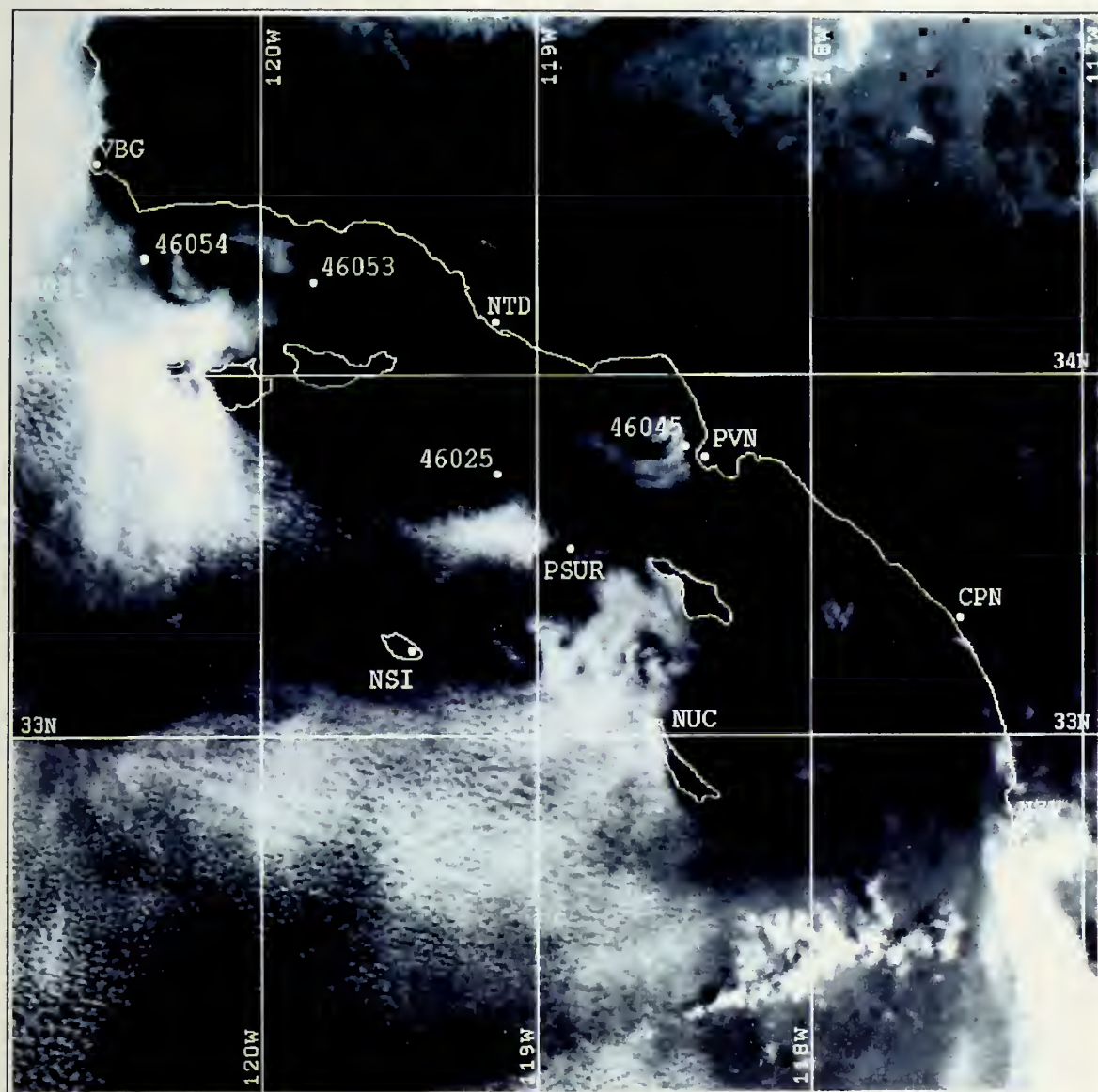


Figure 13: NOAA 12 AVHRR Channel 1 (visible) image of the VOCAR region at 1605z, 27 August, 1993. Locations of all sounding stations and NOAA buoys indicated.

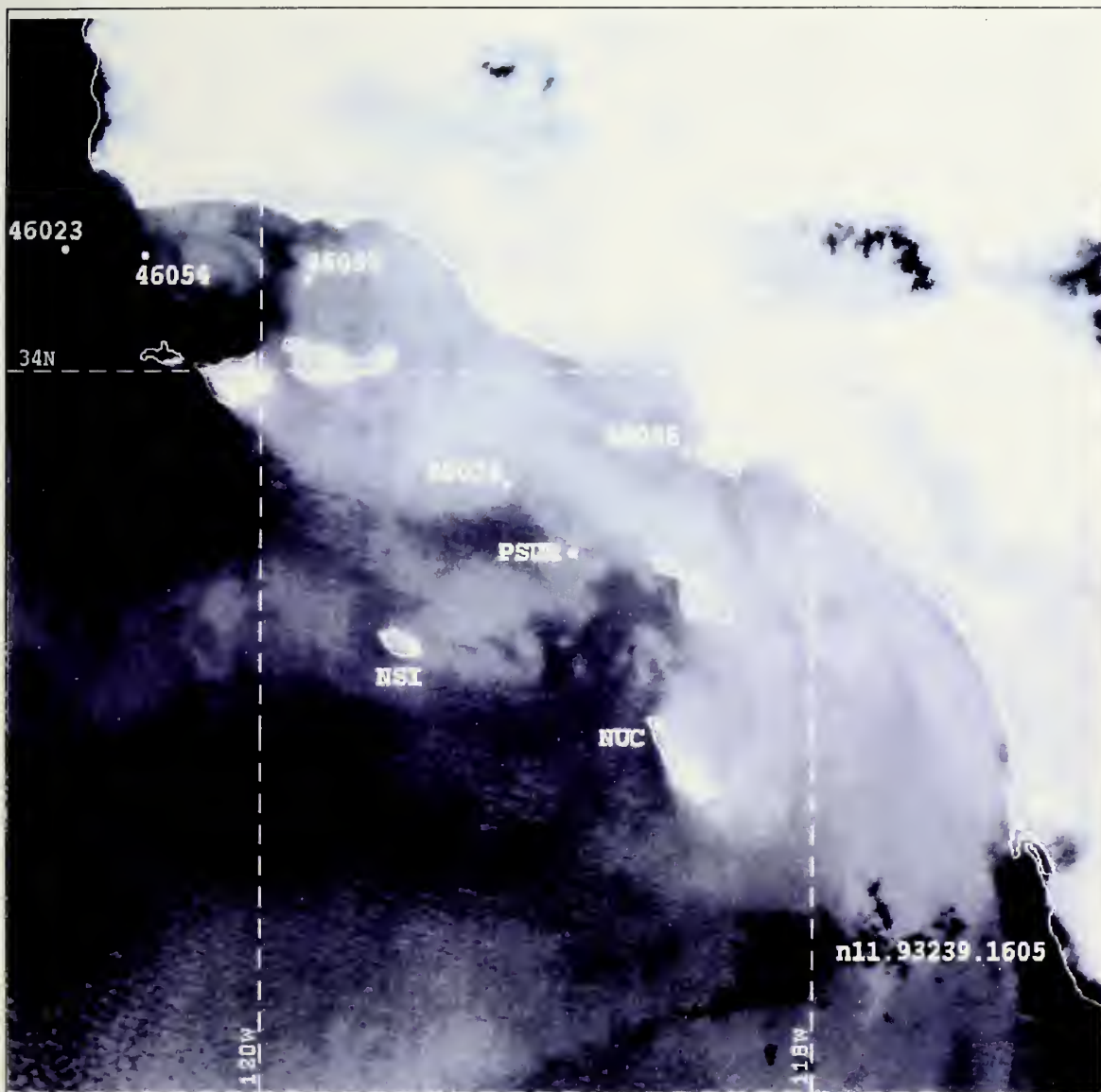


Figure 14: NOAA 12 AVHRR Channel 4 (infrared) image of the VOCAR region at 1605z, 27 August, 1993. The locations of all sounding stations and NOAA buoys indicated.

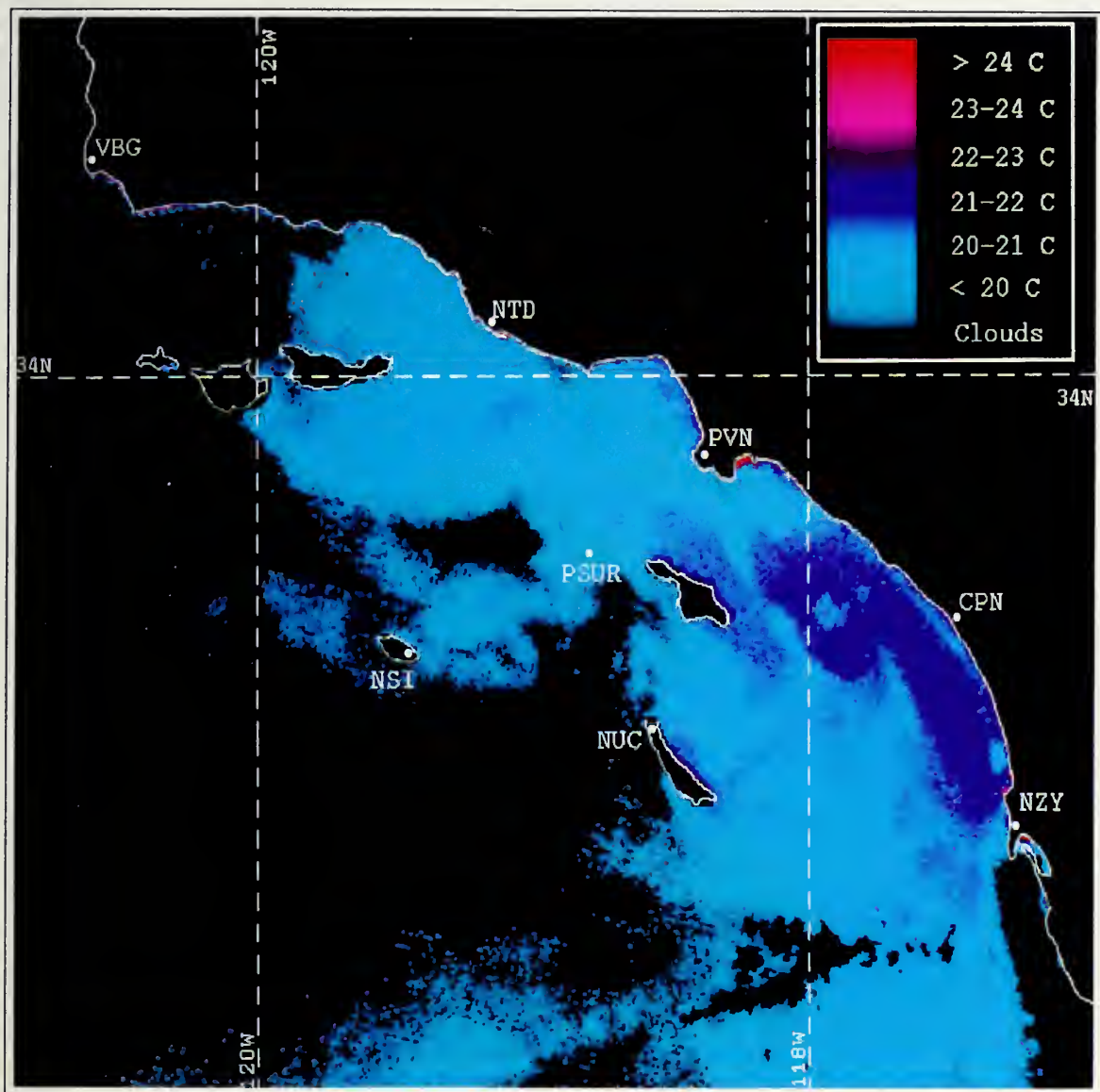


Figure 15: NOAA 12 AVHRR sea surface temperature image of the VOCAR region at 1605z, 27 August, 1993.

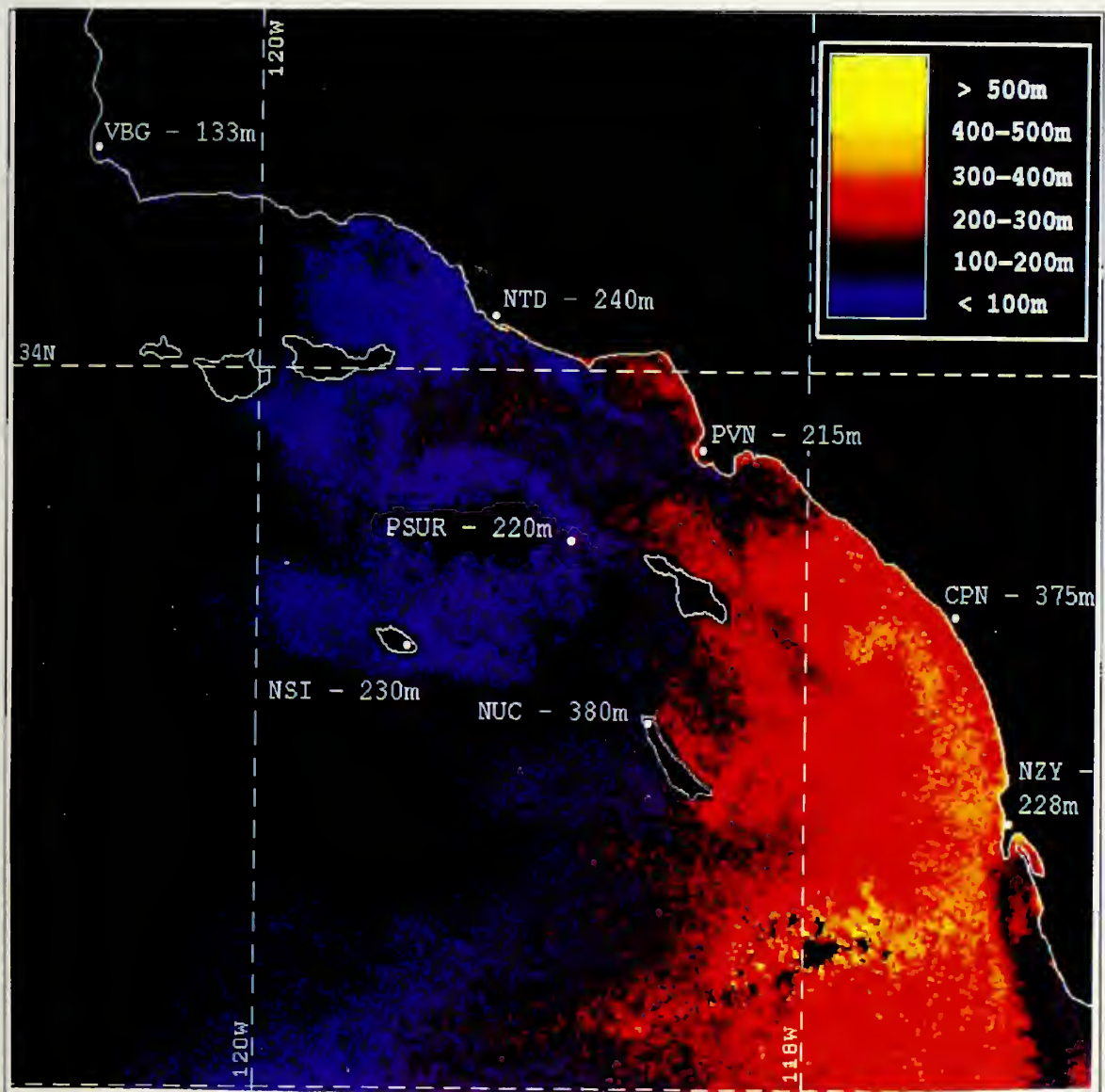


Figure 16: NOAA 12 AVHRR satellite-derived boundary layer height image of the VOCAR region at 1605z, 27 August, 1993. Radiosonde measured BL heights are displayed at each of the launch stations for comparison.

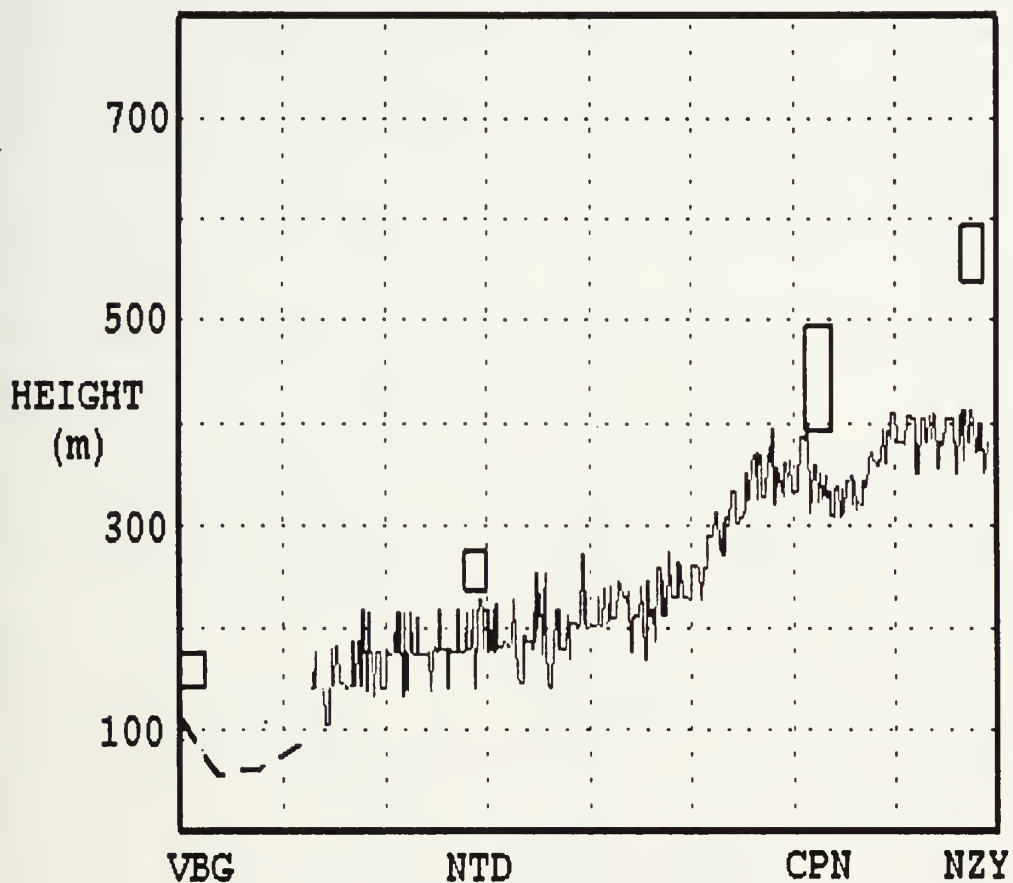


Figure 17: Coastal satellite-derived boundary layer height transect. The vertical axis is height in meters. Boxes represent depth of the trapping layer from radiosonde measurements. Black dashed line = the IR Duct Technique.

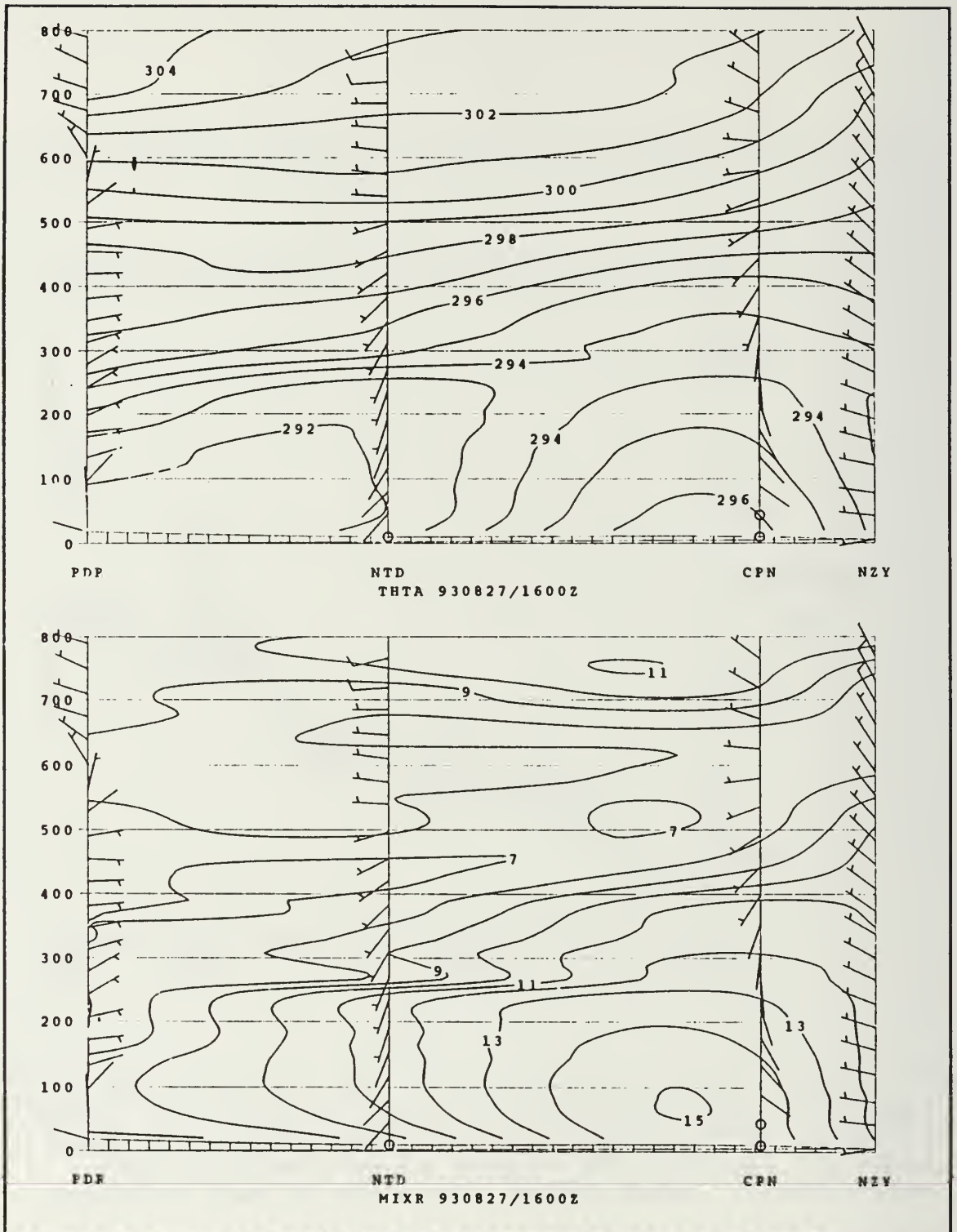


Figure 18: Vertical cross sections of (a) potential temperature (K) and (b) mixing ratio (g/kg) along the coastal transect corresponding to Figure 17. Vertical axis is height in meters.

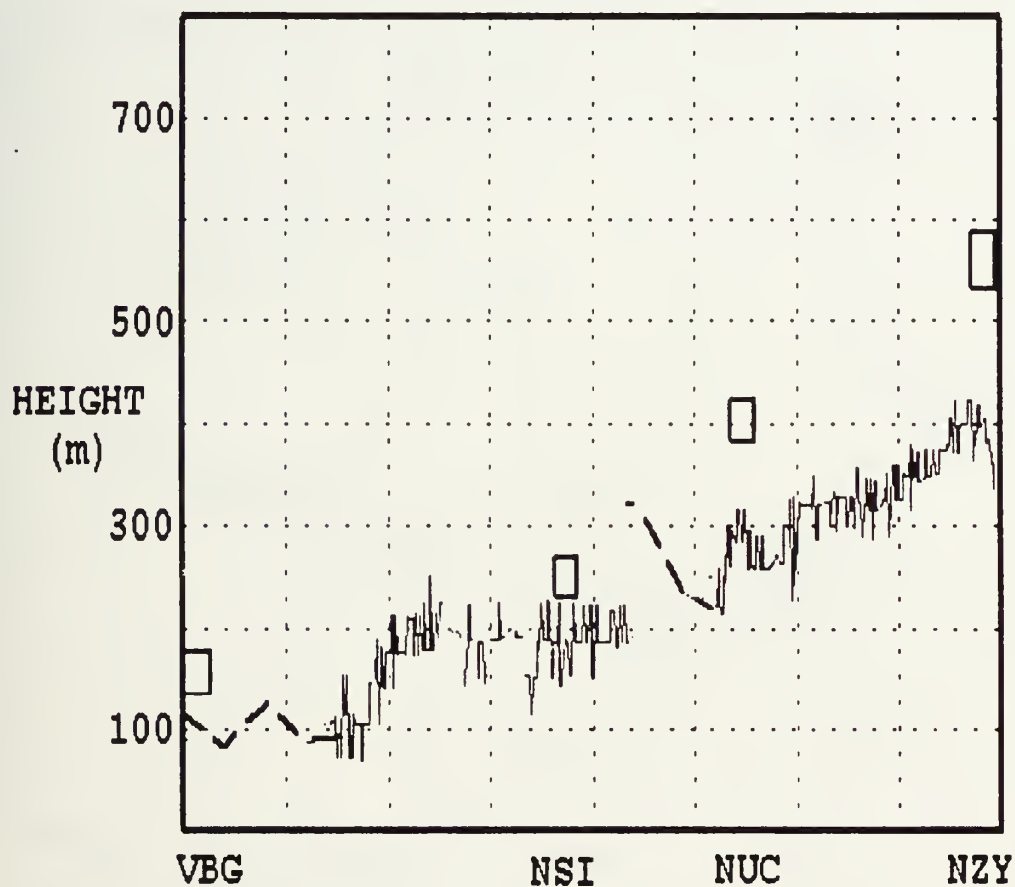


Figure 19: *Offshore* satellite-derived boundary layer height transect. The vertical axis is height in meters. Boxes represent depth of trapping layer from radiosonde measurements. Black dashed lines = IR Duct Technique.

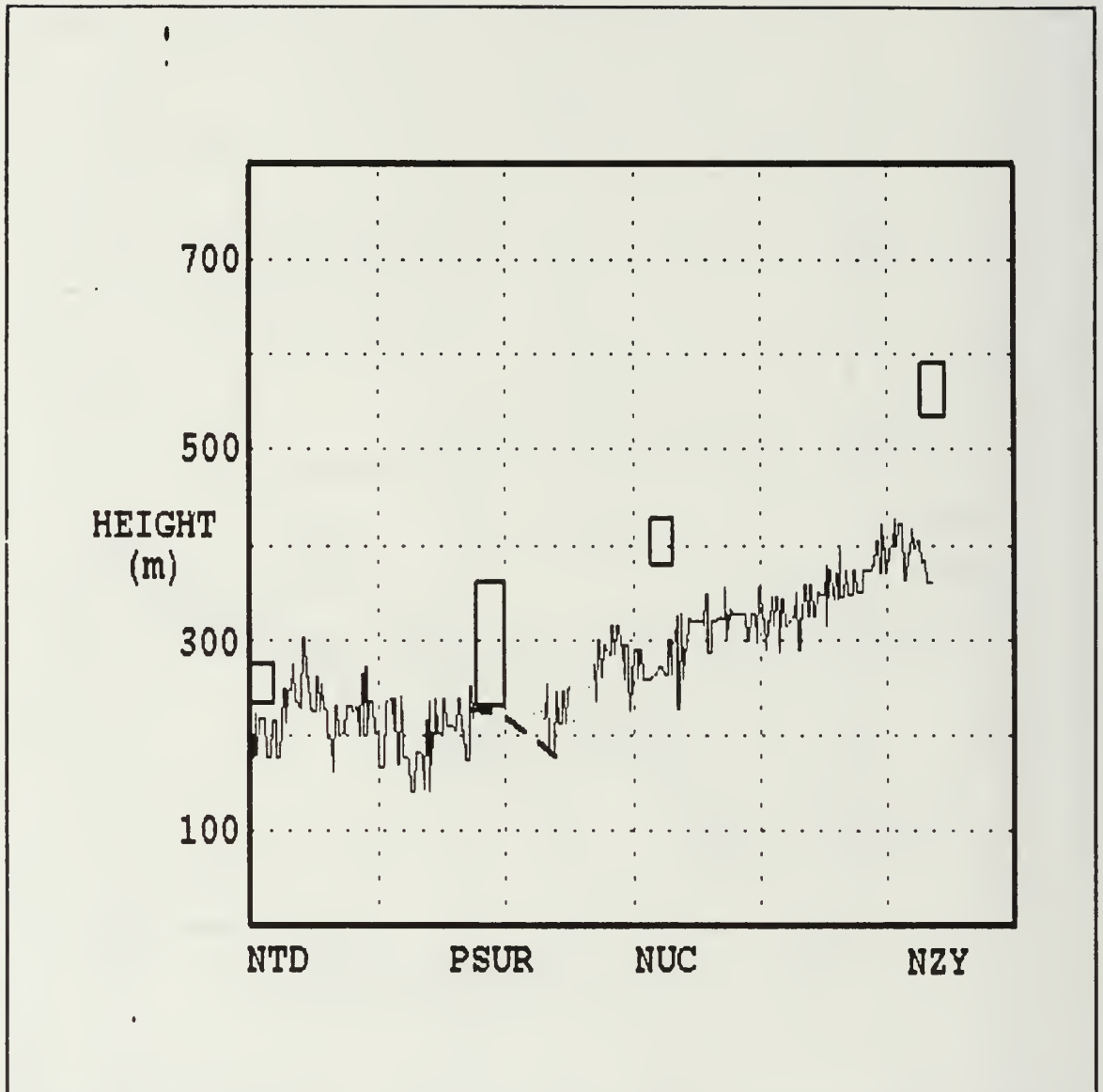
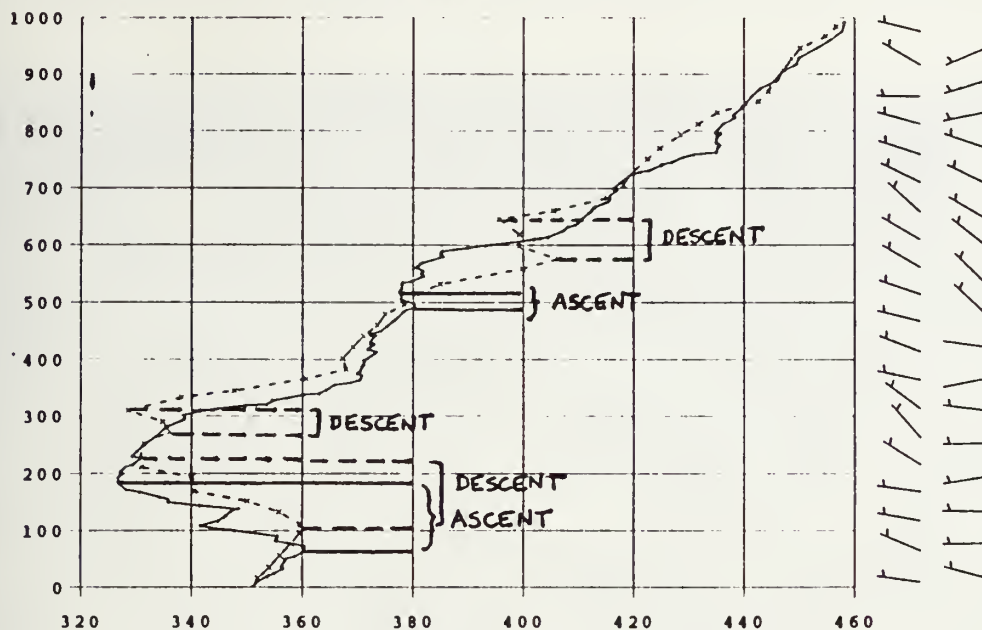


Figure 20: VOCAR satellite-derived boundary layer height transect. Vertical axis is height in meters. Boxes represent depth of the trapping layer from radiosonde measurements. Black dashed line = IR Duct Technique.

930827/1042 0
930827/1123 0

PSUR ascent (+, solid)
PSUR descent (x, dotted)



930827/1432 0
930827/1517 0

PSUR ascent (+, solid)
PSUR descent (x, dotted)

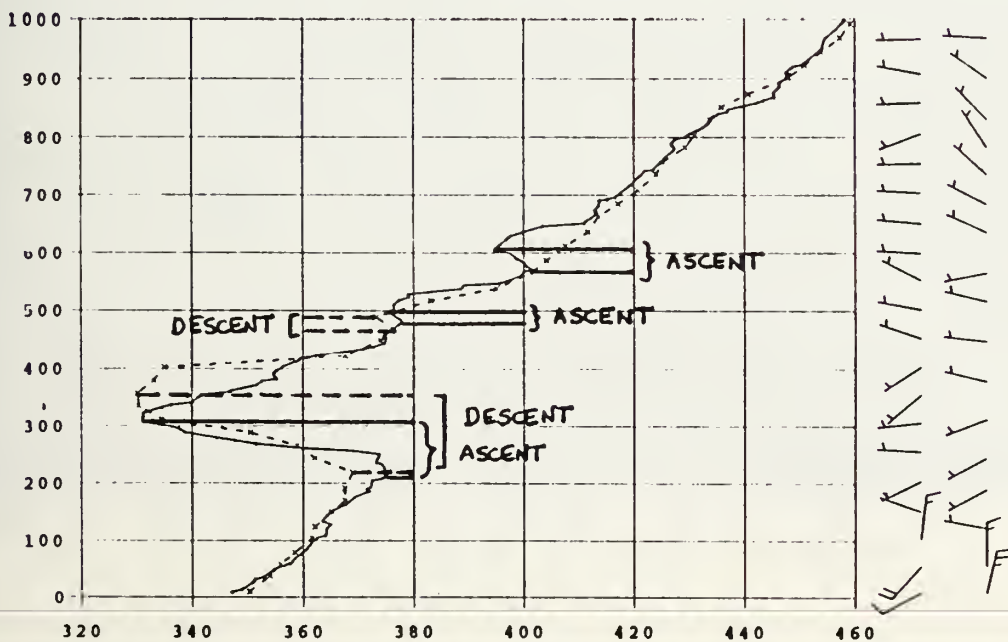


Figure 21: Consecutive up/down soundings from the Pt. Sur on 27 Aug. Times: (a) ascent - solid line @ 1042z, descent - dotted line @ 1123z. (b) ascent - solid line @ 1432z, descent - dotted line @ 1517z. Trapping layers shown.

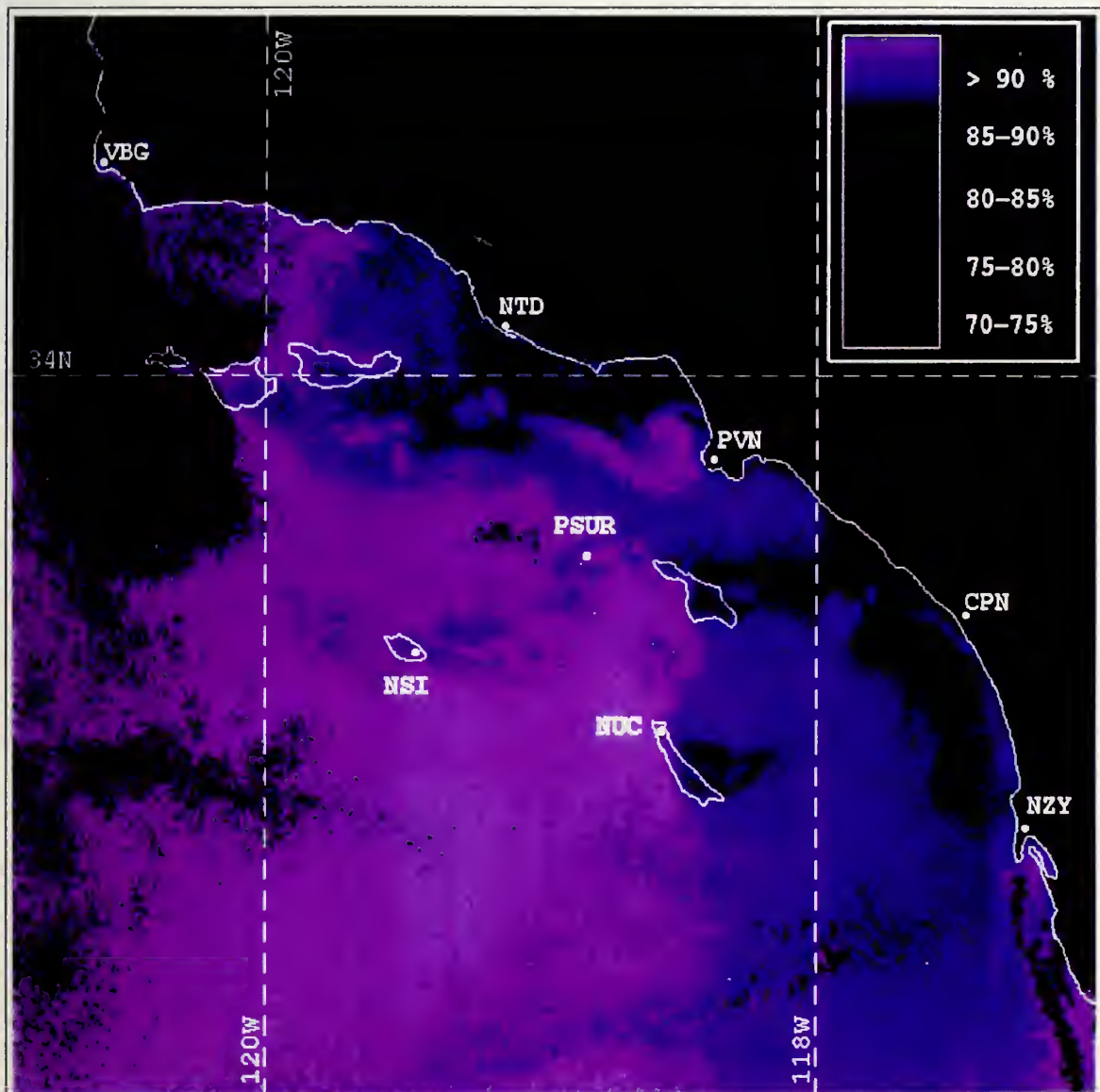


Figure 22: Surface relative humidity image, from the algorithm, of the VOCAR region at 1605z, 27 August, 1993.

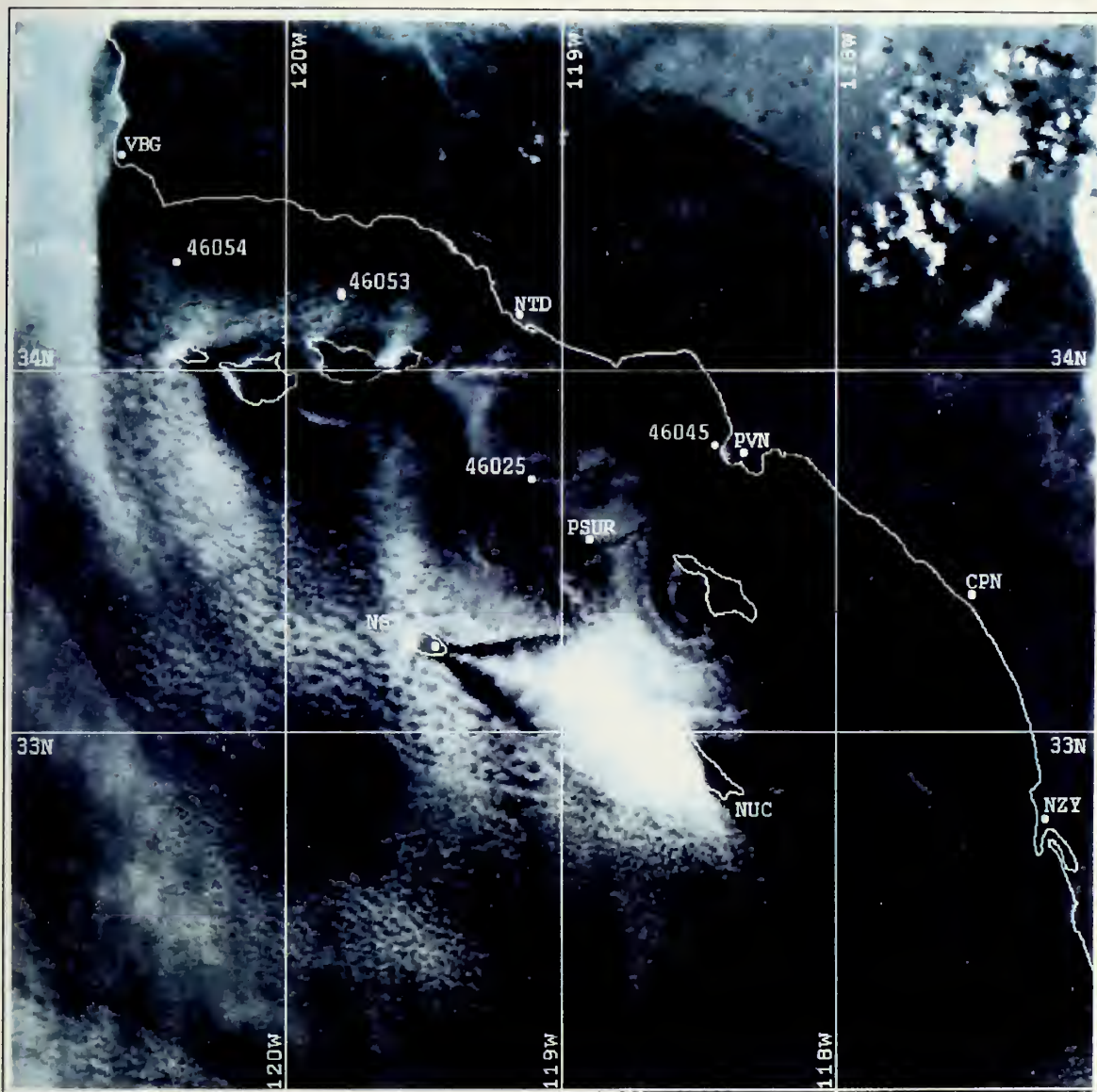


Figure 23: NOAA 11 AVHRR Channel 1 (visible) image of the VOCAR region at 2322z, 28 August, 1993. The location of all sounding stations and NOAA buoys indicated.

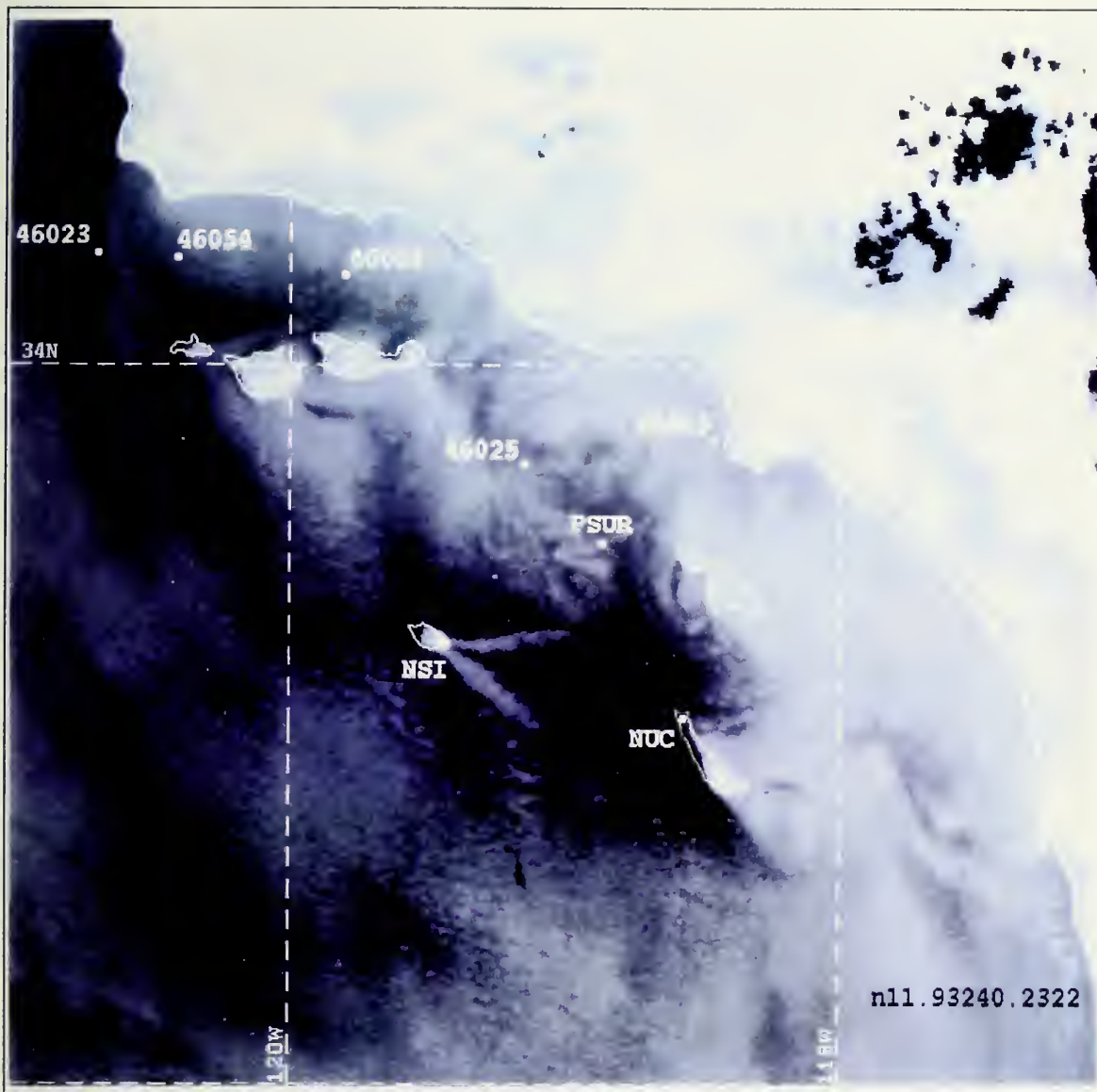


Figure 24: NOAA 11 AVHRR Channel 4 (infrared) image of the VOCAR region at 2322z, 28 August, 1993. The locations of all sounding stations and NOAA buoys indicated.

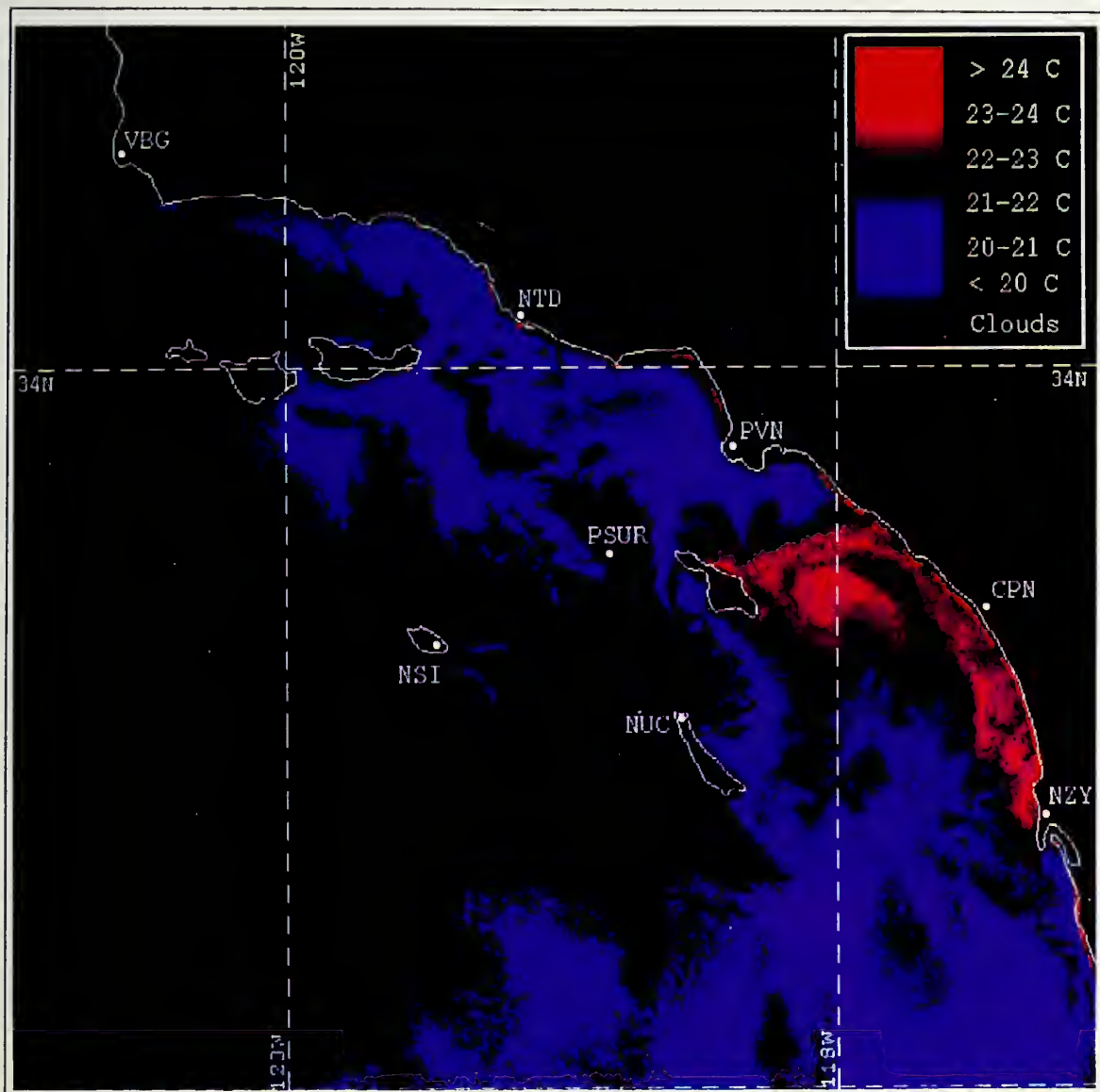


Figure 25: NOAA 11 AVHRR sea surface temperature image of the VOCAR region at 2322z, 28 August, 1993.

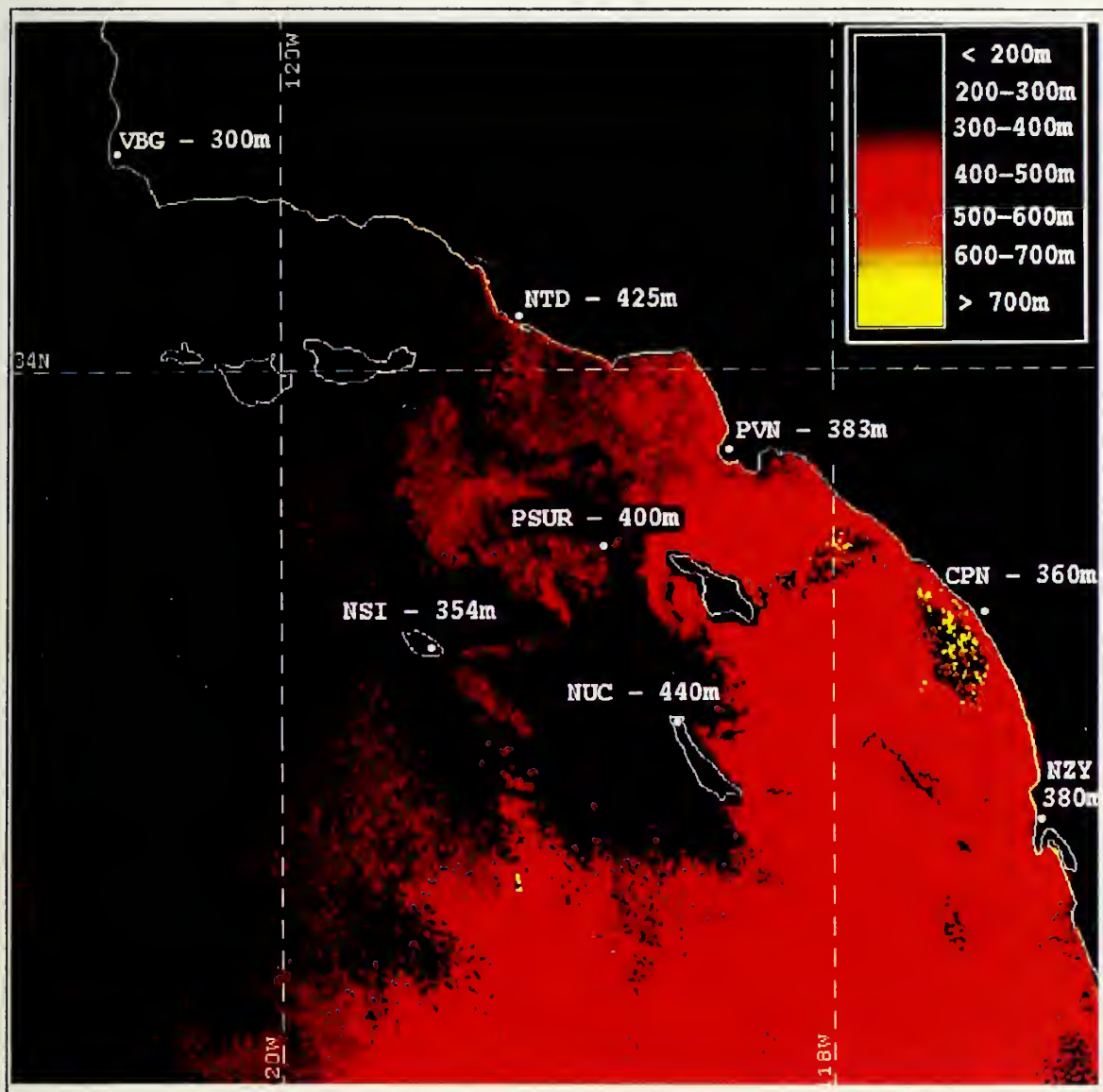


Figure 26: Satellite-derived boundary layer height image of the VOCAR region at 2322z, 28 August, 1993. Radiosonde measured BL heights are displayed at each of the stations for comparison.

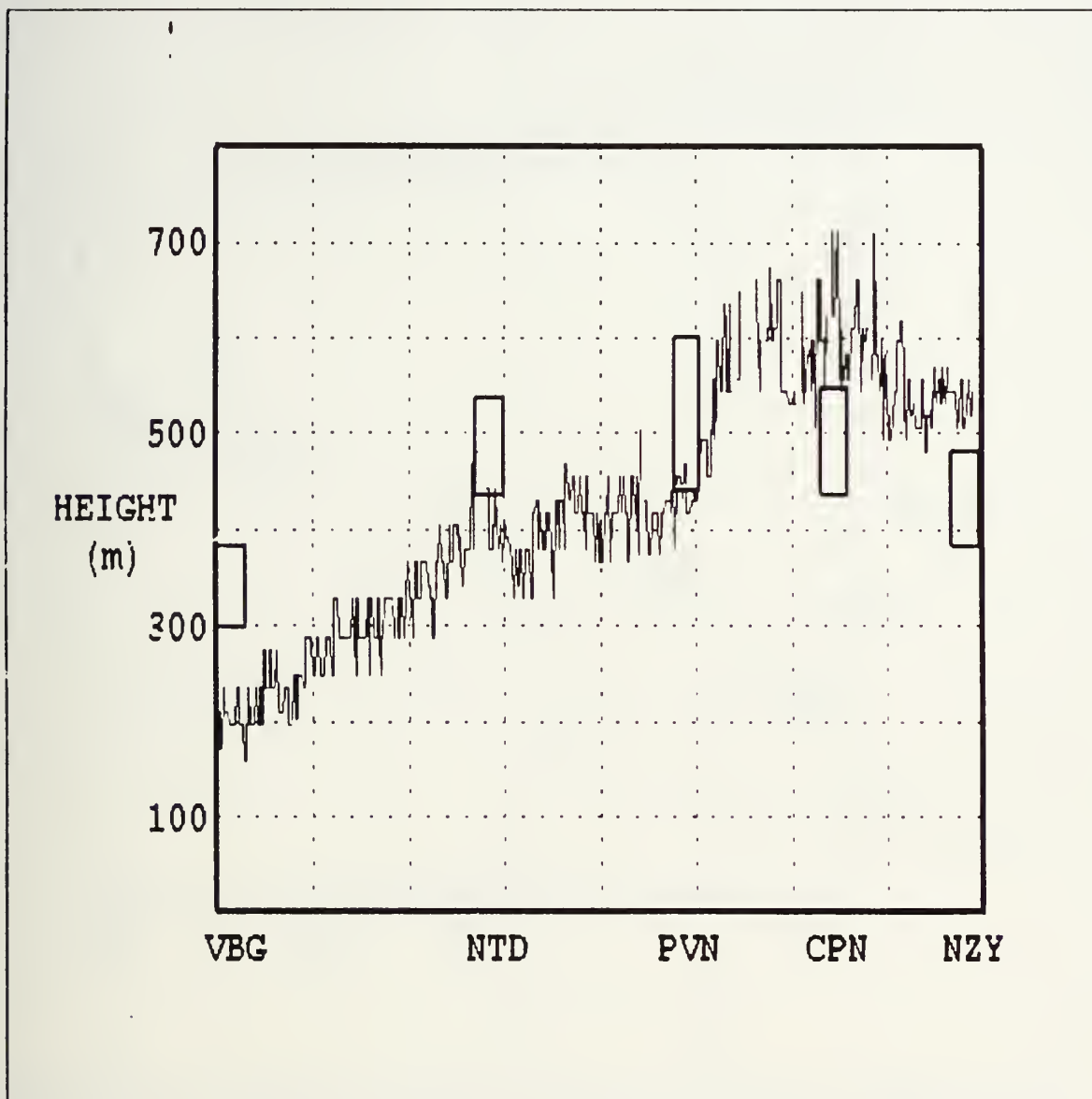


Figure 27: Coastal satellite-derived boundary layer height transect. The vertical axis is height in meters. Boxes represent depth of trapping layer from radiosonde measurements.

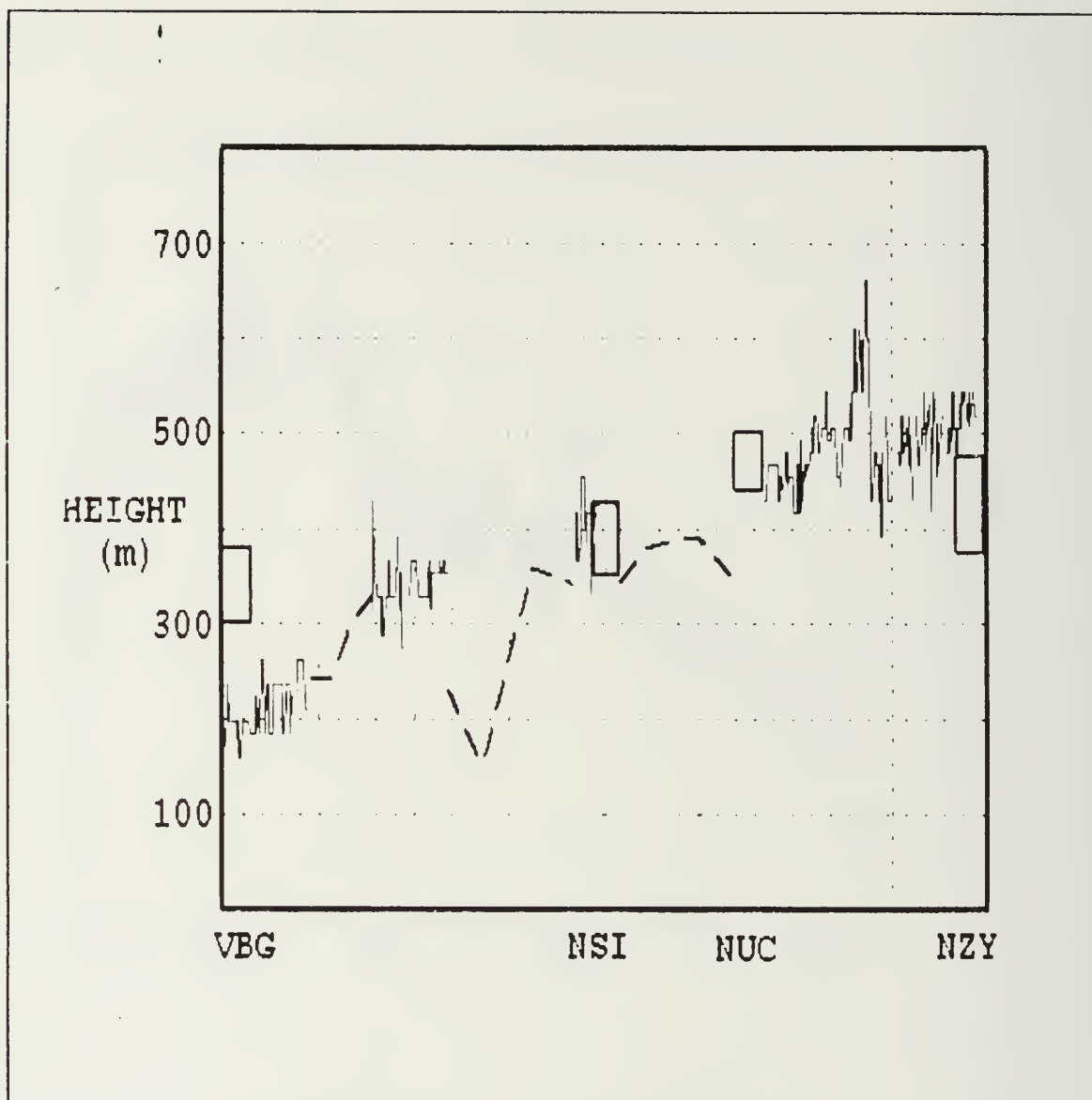


Figure 28: *Offshore* satellite-derived boundary layer height transect. The vertical axis is height in meters. Boxes represent depth of trapping layer from radiosonde measurements. Dashed lines = IR Duct Technique.

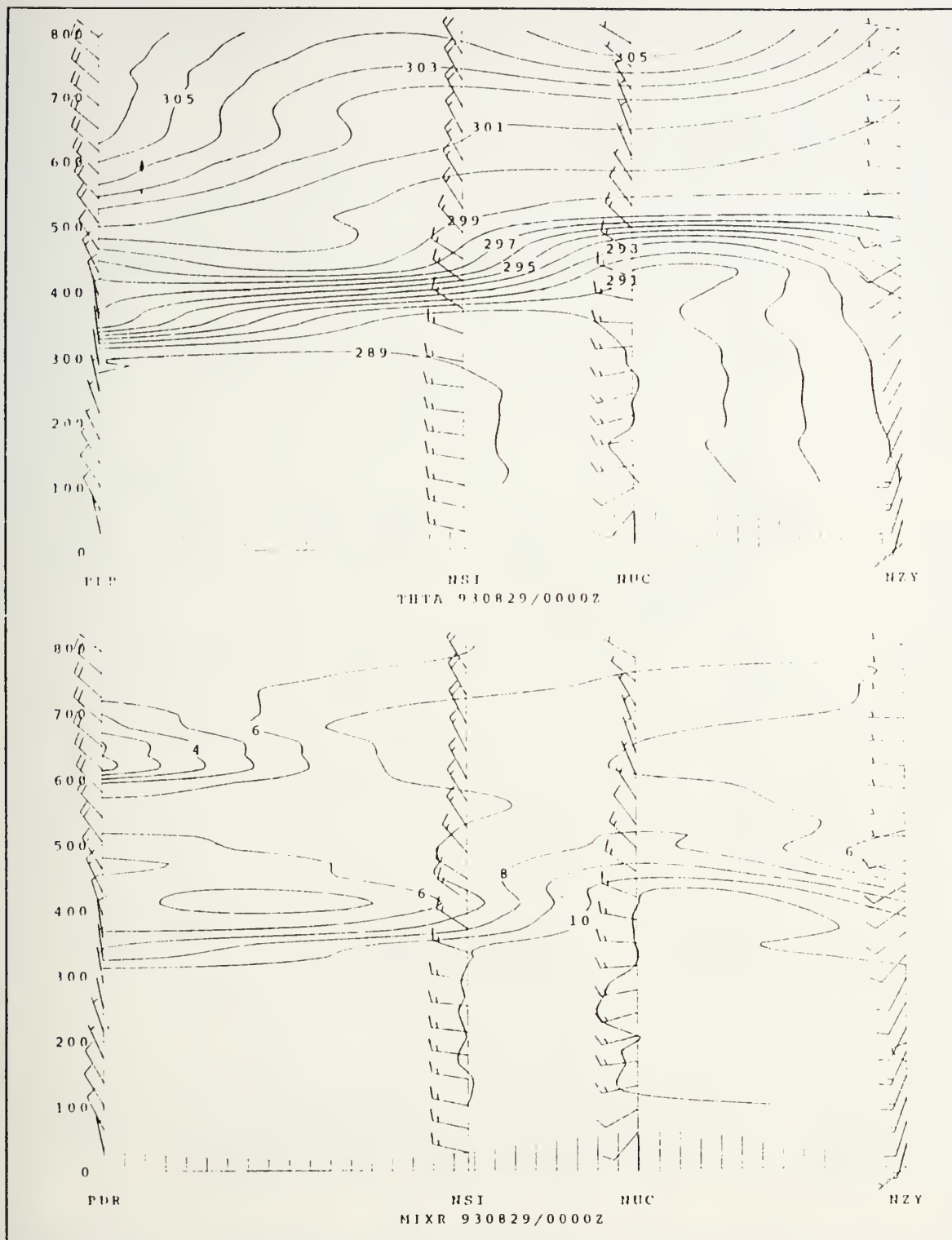


Figure 29: Vertical cross sections of (a) potential temperature (K) and (b) mixing ratio (g/kg) along the **offshore** transect corresponding to Figure 29. Vertical axis is height in meters.

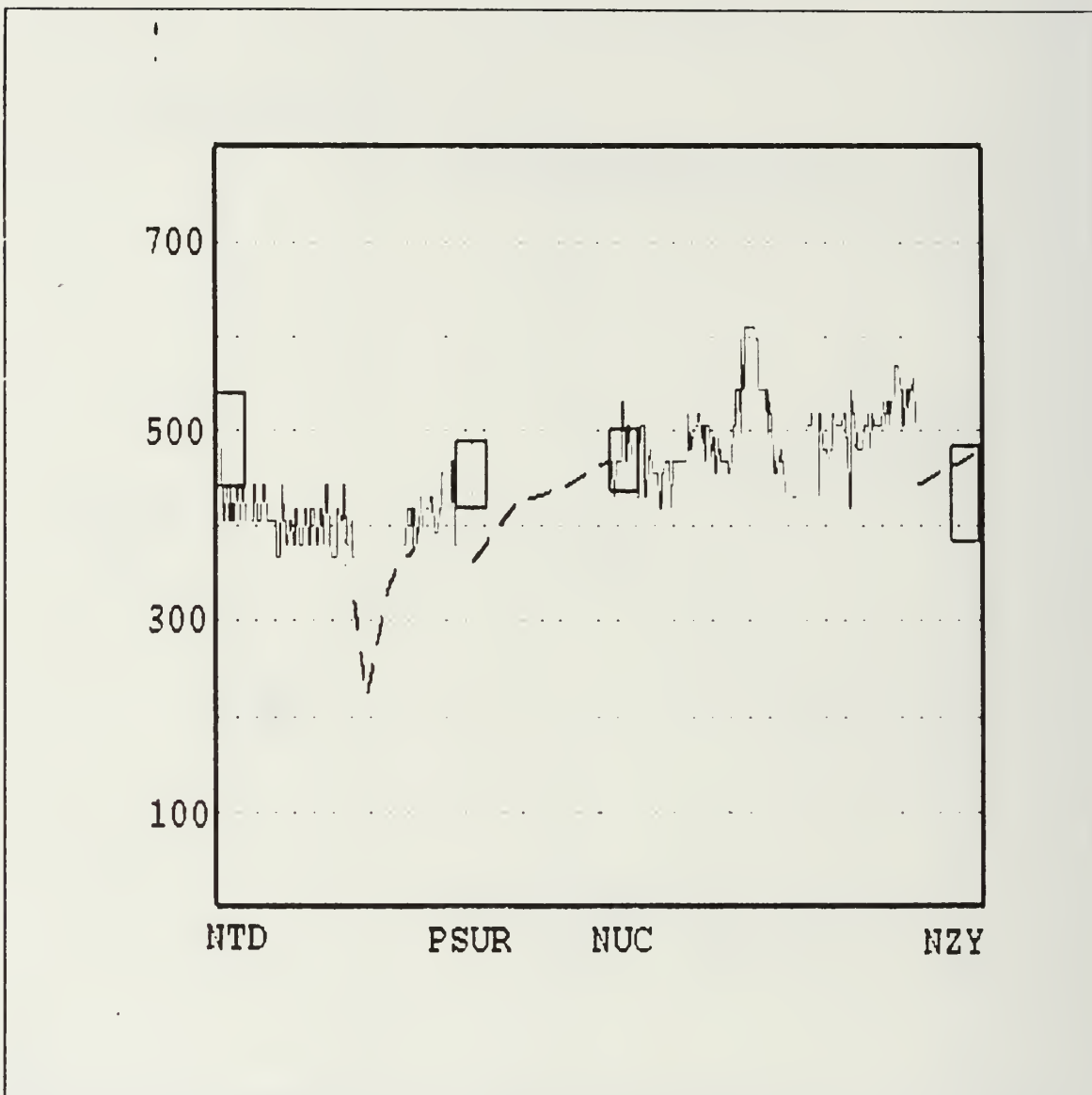


Figure 30: VOCAR satellite-derived boundary layer height transect. The vertical axis is height in meters. Boxes represent depth of trapping layer from radiosonde measurements. Black dashed lines = IR Duct Technique.

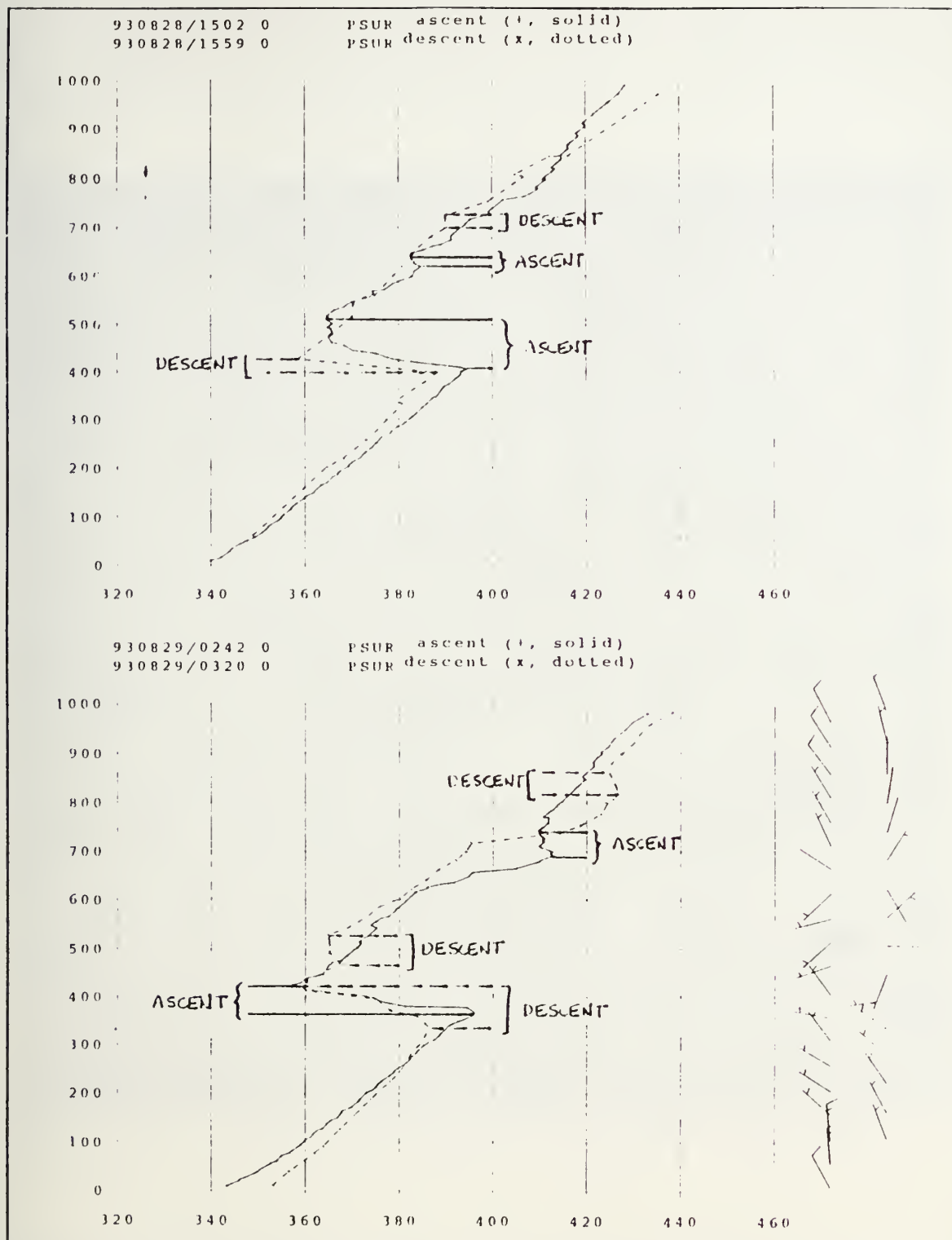


Figure 31: Consecutive up/down soundings from the Pt. Sur on 28/29 Aug. (a) ascent - solid line @ 1502z, descent - dotted line @ 1559z. (b) ascent - solid line @ 0242z, descent - dotted line @ 0320z. Trapping layers shown.

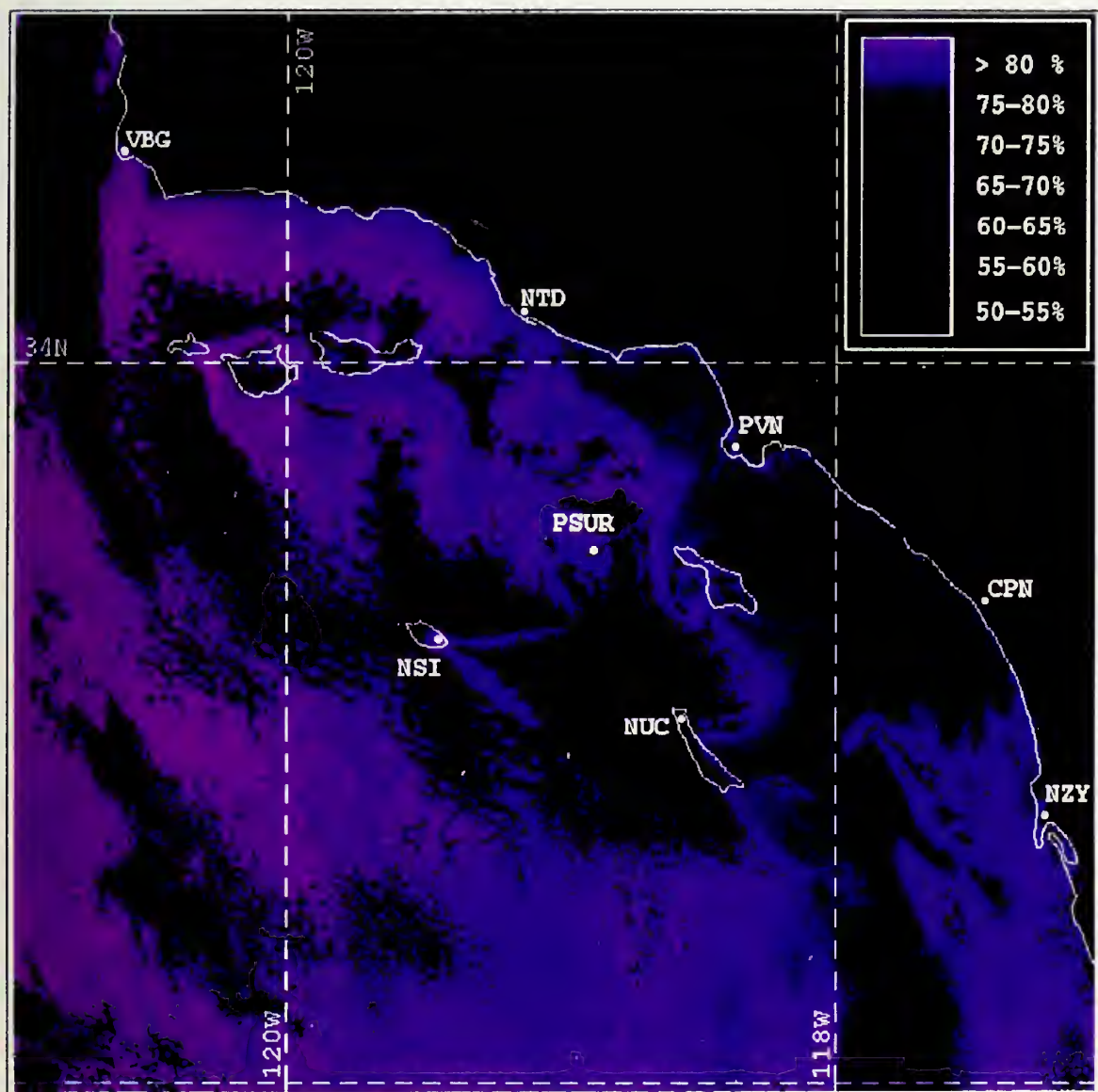


Figure 32: Surface relative humidity image, from the algorithm, of the VOCAR region at 2322z, 28 August, 1993.

Table I: CODE, STATION NAME, LOCATION AND ELEVATION (METERS) OF SURFACE OBSERVATION STATIONS UTILIZED.

VCP7	EMMA WOOD	CA US	3429	-11931	3
SB05	VAFB STS	CA US	3460	-12063	104
SB06	PT ARGUELLO	CA US	3458	-12064	52
SB07	JALAMA BEACH	CA US	3451	-12050	6
SB08	PT CONCEPTION	CA US	3445	-12046	55
SB09	GTCB	CA US	3453	-12020	305
SB10	GAVIOTA WEST	CA US	3448	-12021	91
SB11	GAVIOTA ODOR WEST	CA US	3447	-12022	29
SB12	GTCA	CA US	3447	-12022	29
SB14	GTCC	CA US	3447	-12019	82
SB15	GAVIOTA ODOR EAST	CA US	3447	-12018	35
SB21	WEST CAMPUS LFC10	CA US	3442	-11988	9
SB23	GOLETA	CA US	3445	-11983	50
SB26	CARPENTERIA	CA US	3440	-11946	137
SB27	VAFB WATT RD	CA US	3478	-12061	36
SC05	COSTA MESA	CA US	3365	-11792	25
SC16	LONG BEACH	CA US	3382	-11818	25
SC32	WEST LOS ANGELES	CA US	3405	-11845	96
SD02	OCEANSIDE	CA US	3320	-11737	37
SD03	DEL MAR	CA US	3295	-11726	35
NSIW	SAN NICHOLAS ISLAND	CA US	3326	-11957	9
SCRZ	SANTA CRUZ ISLAND	CA US	3399	-11963	453
SMI	SAN MIGUEL ISLAND	CA US	3403	-12036	253
LGPK	LAGUNA PEAK	CA US	3411	-11906	442
ANCP	ANACAPA ISLAND	CA US	3401	-11936	39
CM06	OCEANSIDE	CA US	3326	-11732	15
CM13	SAN DIEGO	CA US	3273	-11713	113
CM26	GOLETA FOOTHILLS	CA US	3447	-11987	195
CM27	PORT HUENEME	CA US	3417	-11920	5
CM29	SANTA MONICA	CA US	3404	-11848	104

Table II: SEA SURFACE TEMPERATURE COMPARISONS BETWEEN SATELLITE AND 5 BUOYS AS WELL AS THE PT. SUR. TEMPERATURES IN °C.

DATE	FROM	PSUR	46023	46054	46053	46045	46025
27AUG	N12	20.3	15.2	16.9	18.7	19.4	18.9
	BUOY	19.2	14.5	16.5	18.4	20.3	19.0
28AUG	N11	19.4	15.2	17.5	17.3	21.2	20.0
	BUOY	19.6	15.7	16.7	19.0	20.6	20.3

Table III: BOUNDARY LAYER HEIGHT COMPARISONS (SATELLITE VS RADIOSONDE) AT ALL EIGHT STATIONS. HEIGHTS IN METERS.

DATE	FROM	PSUR	NSI	NUC	VBG	NTD	PVN	CPN	NZY
27 AUG	N12	260	165	315	210	290	260	440	340
	RAOB	220	230	380	135	240	215	375	230
28 AUG	N11	395	380	485	185	400	435	570	470
	RAOB	400	355	440	300	425	385	360	380

Table IV: SURFACE RELATIVE HUMIDITY (%) COMPARISONS, SATELLITE VS PT. SUR.

DATE	FROM	PSUR
27AUG	N12	93.7
	SFC OBS	89.7
28AUG	N11	92.3
	SFC OBS	85.1

Table V(a): RESULTS OF APPLYING IR DUCT TECHNIQUE TO CLOUDY AREAS OF THE IMAGE ON 27 AUGUST, 1993. TEMPERATURES IN °C, HEIGHTS IN METERS.

ROUTE	LOCATION	T(cloud)	T(sea)	T(delta)	INV ALT
COASTAL TRANSECT	EAST OF VBG	15.1	16.5	-1.4	108
		16.0	16.5	-0.5	40
		15.9	16.5	-0.6	50
		15.4	16.5	-1.1	85
VOCAR TRANSECT	WNW OF PSUR	16.4	19.2	-2.8	225
		16.5	19.2	-2.7	220
		17.0	19.2	-2.2	175
OFFSHORE TRANSECT	BETWEEN VBG AND SMI	15.1	16.5	-1.4	108
		15.4	16.5	-1.1	85
		15.0	16.5	-1.5	116
		15.4	16.5	-1.1	85
		15.4	16.5	-1.1	85
	BETWEEN NSI AND NUC	15.8	19.2	-3.4	312
		15.8	19.2	-3.4	312
		15.9	19.2	-3.3	302
		16.4	19.2	-2.8	225
		16.6	19.2	-2.6	210

Table V(b); RESULTS OF APPLYING IR DUCT TECHNIQUE TO CLOUDY AREAS OF THE IMAGE ON 28 AUGUST, 1993. TEMPERATURES IN °C, HEIGHTS IN METERS.

ROUTE	LOCATION	T(cloud)	T(sea)	T(delta)	INV ALT
COASTAL TRANSECT	NO GAPS IN SATELLITE DATA ALONG THIS ROUTE				
VOCAR TRANSECT	BETWEEN NTD AND PSUR	16.2	19.6	-3.4	310
		16.9	19.6	-2.7	220
		17.0	19.6	-2.6	210
		15.6	19.6	-4.0	340
		15.1	19.6	-4.5	378
	BETWEEN PSUR AND NUC	15.3	19.6	-4.3	360
		14.6	19.6	-5.0	410
		14.4	19.6	-5.2	430
		14.2	19.6	-5.4	450
	@ NZY	18.2	23.5	-5.3	440
		17.8	23.5	-5.7	485
OFFSHORE TRANSECT	BETWEEN VBG AND SMI	15.6	18.5	-2.9	235
		15.6	18.5	-2.9	235
		15.2	18.5	-3.3	302
		14.9	18.5	-3.6	330
	BETWEEN SMI AND NSI	15.9	18.5	-2.6	210
		16.7	18.5	-1.8	140
		14.4	18.5	-4.1	350
		14.6	18.5	-3.9	329
	BETWEEN NSI AND NUC	14.5	18.5	-4.0	339
		14.0	18.5	-4.5	378
		13.9	18.5	-4.6	390
		14.4	18.5	-4.1	350

LIST OF REFERENCES

- Businger, J.A., 1985: *The Marine Boundary Layer, from Air-Sea Interface to Inversion*. NCAR Technical Note 252, National Center for Atmospheric Research Boulder, CO, 84 pp.
- Dalu, G., Prabhakara, C. and Lo, R.C., 1981: Improved Accuracy of the Remote Sensing of Sea Surface Temperature. In *Oceanography from Space*, edited by J.F.R. Gower, Plenum, New York, N.Y., 109 - 114.
- Dalu, G., 1986: Satellite Remote Sensing of Atmospheric Water Vapor. *Intl. J. Rem. Sens.*, **7**, 1089 - 1097.
- Durkee, P.A., 1984: *The Relationship Between Marine Aerosol Particles and Satellite-Detected Radiance*. Ph.D. Dissertation, Colorado State University, Fort Collins, CO.
- Durkee, P.A., Jensen, D.R., Hindman, E.E., and Vonder Haar, T.H., 1986: The Relationship Between Marine Aerosol Particles and Satellite Detected Radiance. *J. Geo. Res.*, **91**, 4063 - 4072.
- Fitzgerald, J.W., Hoppel, W.A. and Viette, M.A., 1982: The Size and Scattering Coefficient of Urban Aerosol Particles in Washington D.C. as a Function of Relative Humidity. *J. Atm. Sci.*, **39**, 1838 - 1852.
- Geernaert, G.L., 1989: *Remote Sensing of Evaporation Ducts for Naval Warfare*. NRL Report 9228, Naval Research Laboratory, Washington, D.C.
- Gordon, H.R., and Clark, D.K., 1980: Atmospheric Effects in the Remote Sensing of Phytoplankton Pigments. *Boun. Lay. Met.*, **18**, 299 - 313.
- Isaacs, R.G., *Investigation of the Effect of Low-Level Maritime Haze on DMSP VHR and LF Imagery*, 1980: Report CR 80-06, Nav. Environ. Predict. Res. Facil., Monterey, CA.
- Kaufman, Y.J., 1979: Effect of the Earth's Atmosphere on Contrast for Zenith Observations. *J. Geo. Res.*, **84**, 3165-3181.

- Ko, H.W., Sari, J.W. and Skura, J.P., 1983: *Anomalous Microwave Propagation Through Atmospheric Ducts*, Johns Hopkins APL Technical Digest, Vol. 4, No. 3, pp. 12-26.
- Koepke, P., and Quenzel, H., 1981: Turbidity of the Atmosphere Determined by Satellite: Calculation of Optimum Wavelength. *J. Geo. Res.*, **86**, 9801 - 9805.
- Kren, R.J., 1987: *Estimation of Marine Boundary Layer Depth and Relative Humidity with Multispectral Satellite Measurements*. M.S. Thesis, Naval Postgraduate School, Monterey, CA.
- Liou, K.N., 1980: *An Introduction to Atmospheric Radiation*. Academic Press, New York, N.Y., 392 pp.
- Martinez, A.A., 1991: *High Frequency Analyses of Coastal Meteorological Phenomena Affecting Refractivity*. M.S. Thesis, Naval Postgraduate School, Monterey, CA.
- McClain, P., 1985: Comparative Performance of AVHRR-Based Multichannel Sea Surface Temperature. *J. Geo. Res.*, **9**, 11,587 - 11,601.
- McClintock, M., McLellan, A. and Stromovsky, L.A., 1971: *Satellite Measurements of Spectral Turbidity and Albedo, and Their Rates of Change*. Report UWI-SSEC-GAP-71-003, University of Wisconsin, Madison.
- McMillin, L.M., and Crosby, D.S., 1984: Theory and Validation of the Multiple Window Sea Surface Temperature Technique. *J. Geo. Res.*, **89**, 3655 - 3661.
- Nieman, R.A., 1977: *A Comparison of Radiosonde Temperature and Humidity Profile Data Bases*, CSC/TM-77/6133, Contract NAS 5- 11999, Computer Sciences Corp., Silver Spring, MD.
- Paulus, R.A., 1989: *Specification for Environmental Measurements to Assess Radar Sensors*, NOSC Technical Document 1685, Naval Ocean Systems Center, San Diego, CA.
- Prabhakara, C., Dalu, G. and Kunde, V., 1974: Estimation of Sea Surface Temperature from Remote Sensing in the 11 to 13 μ m Window Region. *J. Geo. Res.*, **79**, 5039 - 5044.

- Prabhakara, C., Dalu, G., Lo, R.C. and Nath, N.R., 1979: Remote Sensing of Seasonal Distribution of Precipitable Water Vapor in the Troposphere and it's Meteorological Significance. In *Atmospheric Water Vapor*, Edited by A. Deepak, Academic Press, New York, N.Y., 355 pp.
- Ramsey, R.C., 1968: *Study of the Remote Measurement of Ocean Color*, Final Report, NASW-1658, TRW, Redondo Beach, CA.
- Rogers, R.R., 1979: *A Short Course in Cloud Physics*, Pergamon Press, New York, N.Y., 235 pp.
- Rosenthal, J., and Helvey, R., 1992: *Refractive Assessments from Satellite Observations*, AGARD CP-502, pp. 8.1 - 8.9.
- Shettle, E.P., and Fenn, R.W., 1979: *Models for the Aerosols of the Lower Atmosphere and the Effects of Humidity Variations on their Optical Properties*. AFGL-TR-79-0214, Air Force Geophysics Laboratories, Hanscom AFB, MA, 94 pp.
- Smolinski, S.P., 1988: *Marine Boundary Layer Depth and Relative Humidity Estimates Using Multispectral Satellite Measurements*. M.S. Thesis, Naval Postgraduate School, Monterey, CA.
- Wiscombe, W.J., 1979: *Mie Scattering Calculations: Advances in Technique and Fast, Vector-Speed Computer Codes*, NCAR Tech Note NCAR/TN-140 + STR, National Center for Atmospheric Research, Boulder, CO.
- Wiscombe, W.J., 1980: Improved Mie Scattering Algorithms. *Applied Optics*, 19, 1505-1509.

INITIAL DISTRIBUTION LIST

- | | | |
|-----|---|---|
| 1. | Defense Technical Information Center
Cameron Station
Alexandria, VA 22304-6145 | 2 |
| 2. | Library, Code 052
Naval Postgraduate School
Monterey, CA 93943-5002 | 2 |
| 3. | Chairman (Code MY/HY)
Department of Meteorology
Naval Postgraduate School
Monterey, CA 93943-5114 | 1 |
| 4. | Chairman (Code OC/Co)
Department of Oceanography
Naval Postgraduate School
Monterey, CA 93943-5122 | 1 |
| 5. | Professor Carlyle H. Wash (Code MR/WX)
Department of Meteorology
Naval Postgraduate School
Monterey, CA 93943-5114 | 1 |
| 6. | Professor Kenneth L. Davidson (Code MR/DS)
Department of Meteorology
Naval Postgraduate School
Monterey, CA 93943-5114 | 1 |
| 7. | Lieutenant David J. Walsh
710 Pitt St.
Mt. Pleasant, SC 29464 | 1 |
| 8. | Director Naval Oceanography Division
Naval Observatory
34th and Massachusetts Avenue NW
Washington, DC 20390 | 1 |
| 9. | Commander
Naval Meteorology and Oceanography Command
Stennis Space Center, MS 39529-5000 | 1 |
| 10. | Mr. Jeff Vreugdenhil
20 Broadmoor
Moraga, CA 94556 | 1 |

DUDLEY KNOX LIBRARY



3 2768 00310896 0